

ALMA High-frequency Long Baseline Campaign in 2017:  
Band-to-band Phase Referencing in Submillimeter Waves

YOSHIHARU ASAKI<sup>1,2,3</sup>

LUKE T. MAUD<sup>4,5</sup>

EDWARD B. FOMALONT<sup>1,6</sup>

NEIL M. PHILLIPS<sup>4</sup>

AKIHIKO HIROTA<sup>1,2</sup>

TSUYOSHI SAWADA<sup>1,2</sup>

LORETO BARCOS-MUÑOZ<sup>1,6</sup>

ANITA M. S. RICHARDS<sup>7</sup>

WILLIAM R. F. DENT<sup>1</sup>

SATOKO TAKAHASHI<sup>1,2,3</sup>

STUARTT CORDER<sup>1</sup>

JOHN M. CARPENTER<sup>1</sup>

ERIC VILLARD<sup>1</sup>

ELIZABETH M. HUMPHREYS<sup>4,1</sup>

<sup>1</sup>Joint ALMA Observatory, Alonso de Córdova 3107, Vitacura, Santiago, 763 0355, Chile

<sup>2</sup>National Astronomical Observatory of Japan,

Alonso de Córdova 3788, Office 61B, Vitacura, Santiago, Chile

<sup>3</sup>Department of Astronomical Science, School of Physical Sciences,  
The Graduate University for Advanced Studies (SOKENDAI), 2-21-1 Osawa, Mitaka, Tokyo 181-8588, Japan

<sup>4</sup>ESO Headquarters, Karl-Schwarzschild-Str 2 85748 Garching, Germany

<sup>5</sup>Allegro, Leiden Observatory, Leiden University, PO Box 9513, 2300 RA Leiden, The Netherlands

<sup>6</sup>National Radio Astronomy Observatory, 520 Edgemont Rd. Charlottesville, VA 22903, USA

<sup>7</sup>Jodrell Bank Centre for Astrophysics, Department of Physics and Astronomy,  
University of Manchester, Manchester M13 9PL, UK

(Accepted January 12, 2020)

Submitted to ApJS

ABSTRACT

In 2017, an Atacama Large Millimeter/submillimeter Array (ALMA) high-frequency long baseline campaign was organized to test image capabilities with baselines up to 16 km at submillimeter (submm) wavelengths. We investigated image qualities using ALMA receiver Bands 7, 8, 9, and 10 (285–875 GHz) by adopting band-to-band (B2B) phase referencing in which a phase calibrator is tracked at a lower frequency. For B2B phase referencing, it is expected that a closer phase calibrator to a target

can be used, comparing to standard in-band phase referencing. In the first step, it is ensured that an instrumental phase offset difference between low- and high-frequency Bands can be removed using a differential gain calibration in which a phase calibrator is certainly detected while frequency switching. In the next step, comparative experiments are arranged to investigate the image quality between B2B and in-band phase referencing with phase calibrators at various separation angles. In the final step, we conducted long baseline imaging tests for a quasar at 289 GHz in Band 7 and 405 GHz in Band 8 and complex structure sources of HL Tau and VY CMa at  $\sim 670$  GHz in Band 9. The B2B phase referencing was successfully applied, allowing us to achieve an angular resolution of  $14 \times 11$  and  $10 \times 8$  mas for HL Tau and VY CMa, respectively. There is a high probability of finding a low-frequency calibrator within  $5^\circ.4$  in B2B phase referencing, bright enough to use an 8 s scan length combined with a 7.5 GHz bandwidth.

*Keywords:* Long baseline interferometry (932); Submillimeter astronomy (1647); Phase error (1220);

## 1. INTRODUCTION

The Atacama Large Millimeter/submillimeter Array (ALMA) has been exploring astronomical frontiers with unprecedented angular resolutions and sensitivities in millimeter/submillimeter (mm/submm) waves to observe molecular gas and dust emissions radiated from various astronomical phenomena (Bachiller & Cernicharo 2008). In theory, ALMA can achieve an angular resolution of 15, 9, and 7 mas at observing frequencies of 400, 650, and 850 GHz when baselines of up to 16 km are available. However, using the longest baselines at these frequencies constitutes one of the most challenging observing modes for ALMA.

In order to achieve such high angular resolutions, interferometer phase stabilization of the longest baselines is essential. ALMA long baseline and high-frequency (HF) commissioning, aimed at developing the high angular resolution capabilities, has progressed step-by-step since the construction and commissioning phase. The first moderately extended baseline commissioning test series with respect to the available baselines at the time were made in 2010 before starting Cycle 0 early science by arranging 600 m baselines between one isolated antenna and an antenna cluster distributed in a  $100 \times 100$  m area, in order to evaluate the system-level phase stabilities in ALMA receiver Bands 3, 6, 7, and 9 (Matsushita et al. 2012). In 2012, 2 km baseline experiments were conducted between one isolated antenna and an antenna cluster distributed in a  $500 \times 500$  m area (Matsushita et al. 2014). The first ALMA Long Baseline Campaign (LBC) was organized in 2013 (LBC-2013) for long baseline image capability tests with a maximum of 2.7 km baseline (Asaki et al. 2014; Matsushita et al. 2014; Richards et al. 2014). The second and third ALMA LBCs were organized in 2014 and 2015 (LBC-2014 and LBC-2015), respectively, to accomplish the most extended array configuration with 16 km baselines in order to make science verification (SV) observations in Bands 3, 6, and 7 (ALMA Partnership et al. 2015a,b,c,d), as well as conducting user observations. Phase metrics and phase compensation experiments with baselines up to 16 km were also conducted during the LBCs (Asaki et al. 2016; Hunter et al. 2016; Matsushita et al. 2016). With the success of these campaigns, ALMA has opened 16 km baseline observations to the user community at up to Band 6 frequencies ( $\geq 1.1$  mm wavelength, or  $\leq 275$  GHz) in Cycle 6, regularly achieving angular resolutions of 18 mas. In 2014, some observations were made in Band 7 on 16 km baselines at angular resolutions of  $\sim 20$  mas in Cycle 3 (e.g. Andrews et al. 2016; Kervella et al. 2016), and most recently, Band 7 16 km baseline observations have been opened up since Cycle 7.

At ALMA, state-of-the-art technologies are used for stabilizing instrumental phases in signal paths required for mm/submm interferometer observations (Bryerton et al. 2005; Cliche & Shillue 2006). Nevertheless, the phase stability throughout the whole observing system cannot be well controlled because the largest error is caused by Earth's atmosphere, particularly, water vapor in the lower troposphere (Robson et al. 2001). Accurate phase correction, to compensate for the atmospheric phase errors, is mandatory to perform ALMA long baseline observations at the highest frequencies. One of the key techniques to correct atmospheric water vapor phase errors is to use a water vapor radiometer (WVR; Nikolic et al. 2013, and references therein) equipped on each 12 m antenna. Since the opacity of the atmospheric water vapor at 183 GHz has a strong correlation with the mm/submm wave excess path length at the Atacama site, the opacity measured with the WVRs can be used to derive precipitable water vapor (PWV) content every few seconds and thus derive corrections for the associated phase fluctuations.

Phase referencing is another important technique for interferometer phase correction (e.g. Beasley & Conway 1995; Asaki et al. 2007). A nearby quasar (QSO) is used as a phase calibrator by being observed alternately with the science

target. This is used to calibrate phase errors due to instrumental phase offsets and mitigate antenna position errors, as well as correcting residual atmospheric phase fluctuations after the WVR phase correction. Phase referencing using a phase calibrator at the same frequency of the target is referred to as in-band phase referencing. This is the general phase correction technique for all interferometers and has been adopted at ALMA as a standard phase correction method, along with WVR phase correction. The combination of the above two techniques is quite successful for the phase correction in ALMA (Matsushita et al. 2017).

Note that an extension to phase referencing known as fast switching, is one in which a phase calibrator is observed with a cadence of a few tens of seconds. If a rapid phase change causes  $2\pi$  phase wrappings between the phase calibrator scans, we are unable to track whether the phases are moving positively or negatively from the previous scan. The ALMA antennas can quickly change their position by several degrees in a few seconds to accommodate such a mode, which is most important for HFs where the atmospheric fluctuations are most variable.

In the submm wave regime (wavelength  $<1$  mm, roughly ALMA Band 7 and higher frequencies), several factors make in-band phase referencing increasingly difficult. Since the atmospheric phase errors are mainly caused by an excess delay change, phase corrections must be made more frequently using the fast switching technique, and the phase calibrator must be at a smaller separation angle from the target. However, as the observing frequency increases, the flux densities of most QSOs diminish, and the system noise temperature rises. This indicates that fewer bright-enough phase calibrators are available close to targets at arbitrary sky positions.

To alleviate the difficulty, the so-called band-to-band (B2B) phase referencing technique is considered to be an alternative phase correction method in which a phase calibrator is observed at a lower frequency. Since the interferometer phase error is almost proportional to the observing frequency (see also Section 2.1), the phase corrections derived from the phase calibrator at a low frequency (LF) can be multiplied by a ratio of the HF and LF and applied to the phases of the HF target. The B2B phase referencing technique was first demonstrated using the Nobeyama Millimeter Array between 148 and 19.5 GHz for a target QSO and a reference communication satellite (Asaki et al. 1998). In B2B phase referencing, it is necessary to remove any instrumental phase offset difference between the two frequencies. A similar multifrequency phase correction has been made for the Combined Array for Research in Millimeter-wave Astronomy (CARMA) science array at 227 GHz using a nearby calibrator’s interferometer delay measurements at 30.4 GHz obtained with a reference antenna array and applied to the target using the CARMA pair antenna calibration system (C-PACS; Pérez et al. 2010; Zauderer et al. 2016). In C-PACS, the instrumental phase offset difference was corrected by applying a phase difference between the two arrays when they observed the same phase calibrator simultaneously. Another realization of such a multifrequency phase referencing is made in the Korean very long baseline interferometry (VLBI) network, which can observe at 22, 43, 86, and 129 GHz simultaneously (Dodson et al. 2014; Rioja et al. 2014) with quasi-optics in the receiver (Han et al. 2013).

In order to offer new ALMA image capabilities at the highest angular resolutions, implementation of B2B phase referencing is crucial. This was the focus of the fourth long baseline capability campaign organized in 2017. This paper presents results from our feasibility study made during the High Frequency Long Baseline Campaign 2017 (HF-LBC-2017). We aimed to prove that ALMA has observation capabilities in Bands 7, 8, 9, and 10 (285–875 GHz) with up to the longest 16 km baselines using B2B phase referencing. Section 2 mentions the basic concept of B2B phase referencing, while Section 3 introduces the strategy of HF-LBC-2017. The main results of HF-LBC-2017 are presented in Section 4. The availability of the phase calibrator for B2B and in-band phase referencing is discussed in Section 5. We summarize the overall feasibility study in Section 6. Note that the details of parts of the experiments are described in additional relevant papers (Asaki et al. 2019; Maud, L. T. et al. in preparation)

## 2. BASIC CONCEPT OF B2B PHASE REFERENCING

The main goal of interferometer phase correction is to remove systematic phase errors due to errors of instrumental electrical path length and a priori antenna position and to improve the coherence of the visibilities disturbed by atmospheric phase fluctuations. Our basic phase correction procedure for HFs on long baselines is divided into WVR phase correction and B2B phase referencing. The WVR phase correction and its performance are described in previous reports (Matsushita et al. 2017; Maud et al. 2017) and references therein. The effectiveness of phase referencing for ALMA was previously investigated for in-band phase referencing in Band 3 and B2B phase referencing in Band 7 with phase calibrators in Band 3 (Asaki et al. 2014, 2016). Such phase referencing techniques for switching between a target and phase calibrator allow very accurate tracking of the rapid atmospheric phase fluctuations and can effectively remove the phase errors, especially for baselines longer than several kilometers. In cases of narrow-bandwidth science

observations for targeting specific molecular lines, phase calibrators are observed in a wider-bandwidth mode in order to obtain higher signal-to-noise ratios (S/Ns). The combination of the above bandwidth switching and B2B phase referencing may provide more flexibility in ALMA HF observations for molecular lines. In this section, we describe the basic concept of B2B phase referencing and relevant ideas regarding its implementation in HF-LBC-2017.

### 2.1. B2B phase referencing

Figure 1 shows a typical observation sequence of B2B phase referencing. A phase referencing block consists of alternately pointing at a phase calibrator, observed at an LF  $\nu_{\text{LF}}$ , and at a target source, observed at an HF  $\nu_{\text{HF}}$ . A differential gain calibration (DGC) source is observed alternately at both frequencies for calibrating the instrumental phase offset difference later described in Section 2.2. Other standard calibration scans to measure the system noise temperature, as well as bandpass calibration, pointing calibration, and flux calibration, are also prepared for the HF target. We express observed interferometer phases  $\Phi^{\text{T}}$  and  $\Phi^{\text{C}}$  at  $\nu_{\text{HF}}$  of the target and at  $\nu_{\text{LF}}$  of the phase calibrator, respectively, as follows:

$$\begin{aligned}\Phi^{\text{T}}(t) &= \Phi_{\text{total}}^{\text{T}}(t) - \Phi_{\text{apri}}^{\text{T}}(t) \\ &= 2\pi\nu_{\text{HF}} [\tau_{\text{trp}}^{\text{T}}(t) + \tau_{\text{bl}}^{\text{T}}(t)] + \frac{2\pi\kappa}{c\nu_{\text{HF}}} \Delta\text{TEC}^{\text{T}}(t) \\ &\quad + \Phi_{\text{inst-H}}^{\text{T}}(t) + \Phi_{\text{vis-H}}^{\text{T}}(t) + \Phi_{\text{therm-H}}^{\text{T}}(t),\end{aligned}\tag{1}$$

$$\begin{aligned}\Phi^{\text{C}}(t') &= \Phi_{\text{total}}^{\text{C}}(t') - \Phi_{\text{apri}}^{\text{C}}(t') \\ &= 2\pi\nu_{\text{LF}} [\tau_{\text{trp}}^{\text{C}}(t') + \tau_{\text{bl}}^{\text{C}}(t')] + \frac{2\pi\kappa}{c\nu_{\text{LF}}} \Delta\text{TEC}^{\text{C}}(t') \\ &\quad + \Phi_{\text{inst-L}}^{\text{C}}(t') + \Phi_{\text{vis-L}}^{\text{C}}(t') + \Phi_{\text{therm-L}}^{\text{C}}(t'),\end{aligned}\tag{2}$$

where

$\Phi_{\text{total}}$  is the total interferometer phase in summation of geometrical delays and all errors;

$\Phi_{\text{apri}}$  is the a priori phase calculated in the correlator including contributions of the WVR phase correction;

$\tau_{\text{trp}}$  is the atmospheric delay error;

$\tau_{\text{bl}}$  is the delay error due to the baseline vector error coming from the geometrical uncertainties of the antenna positions and uncertainties of the Earth orientation parameters;

$\Delta\text{TEC}$  is the spatial difference of the total electron content (TEC) of the ionosphere in the line of sight between two antennas ( $\kappa = 40.3 \text{ m}^3 \text{ s}^{-2}$ );

$\Phi_{\text{inst-H}}$  and  $\Phi_{\text{inst-L}}$  are the instrumental phase offsets of frequency standard signals at  $\nu_{\text{HF}}$  and  $\nu_{\text{LF}}$ , respectively;

$\Phi_{\text{vis-H}}^{\text{T}}$  and  $\Phi_{\text{vis-L}}^{\text{C}}$  are the visibility phases representing the target source structure at  $\nu_{\text{HF}}$  and the phase calibrator at  $\nu_{\text{LF}}$ , respectively, with respect to their a priori phase tracking centers; and

$\Phi_{\text{therm-H}}$  and  $\Phi_{\text{therm-L}}$  are the thermal noises at  $\nu_{\text{HF}}$  and  $\nu_{\text{LF}}$ , respectively.

Superscripts T and C denote target and phase calibrator, and  $c$  is the speed of light. Here the target and phase calibrator are temporally observed in sequence. For simplification, let us assume that the target and phase calibrator are both point sources at their respective frequencies located at their a priori phase tracking centers ( $\Phi_{\text{vis-H}}^{\text{T}} = \Phi_{\text{vis-L}}^{\text{C}} = 0$ ). We denote that the mid-time point of the target and phase calibrator scans in one sequence occur at  $t$  and  $t'$ , respectively. One important parameter of this sequence is called a switching cycle time, which is a length of time denoted  $t_{\text{swt}}$ . This can be understood as the interval from the phase calibrator scan midpoint at  $t'$  to the next scan midpoint of the phase calibrator at  $t' + t_{\text{swt}}$ . Thus,  $t_{\text{swt}}$  encompasses the time spent on the calibrator and target and slewing overheads twice between the two. In order to correct  $\Phi^{\text{T}}$ , a correcting phase  $\Phi_{\text{cal}}^{\text{C}}$  at time  $t$  is obtained by averaging  $\Phi^{\text{C}}$  (the temporally closest two phase calibrator scans of Equation (2)) and multiplying by an observing frequency ratio  $R = \nu_{\text{HF}}/\nu_{\text{LF}}$  as follows:

$$\begin{aligned}\Phi_{\text{cal}}^{\text{C}}(t) &= \frac{\nu_{\text{HF}}}{\nu_{\text{LF}}} \cdot \frac{\Phi^{\text{C}}(t - t_{\text{swt}}/2) + \Phi^{\text{C}}(t + t_{\text{swt}}/2)}{2} \\ &\simeq 2\pi\nu_{\text{HF}} \left[ \overline{\tau_{\text{trp}}^{\text{C}}}(t) + \overline{\tau_{\text{bl}}^{\text{C}}}(t) \right] + R \left[ \frac{2\pi\kappa}{c\nu_{\text{LF}}} \overline{\Delta TEC^{\text{C}}}(t) + \overline{\Phi_{\text{inst-L}}^{\text{C}}}(t) + \overline{\Phi_{\text{therm-L}}^{\text{C}}}(t) \right].\end{aligned}\quad (3)$$

This procedure is referred to as frequency phase transfer (Rioja et al. 2014). The B2B phase referencing is carried out by subtracting  $\Phi_{\text{cal}}^{\text{C}}$  of Equation (3) from Equation (1) as follows:

$$\begin{aligned}\Phi^{\text{T}}(t) - \Phi_{\text{cal}}^{\text{C}}(t) &= 2\pi\nu_{\text{HF}} \left[ \tau_{\text{trp}}^{\text{T}}(t) - \overline{\tau_{\text{trp}}^{\text{C}}}(t) \right] + 2\pi\nu_{\text{HF}} \left[ \tau_{\text{bl}}^{\text{T}}(t) - \overline{\tau_{\text{bl}}^{\text{C}}}(t) \right] \\ &\quad + \left[ \Phi_{\text{therm-H}}^{\text{T}}(t) - R \overline{\Phi_{\text{therm-L}}^{\text{C}}}(t) \right] \\ &\quad + \frac{2\pi\kappa}{c\nu_{\text{HF}}} \left[ \Delta TEC^{\text{T}}(t) - R^2 \overline{\Delta TEC^{\text{C}}}(t) \right] + \left[ \Phi_{\text{inst-H}}^{\text{T}}(t) - R \overline{\Phi_{\text{inst-L}}^{\text{C}}}(t) \right].\end{aligned}\quad (4)$$

A pervasive concern regarding B2B phase referencing is a dispersive term of mm/submm wave delay refraction of the atmospheric water vapor. The assumption of the nondispersiveness is likely to be correct except close to strong atmospheric water vapor absorption lines (Pardo et al. 2001). Figure 2 depicts a relative dispersive delay between the dispersive and nondispersive terms of the atmospheric water vapor at the ALMA site (PWV=1 mm) calculated with the ALMA ATM program (Nikolic 2009) and the ALMA bands. Although HF observations are conducted in low-PWV conditions (typically,  $\leq 1$  mm in Band 8), we have to take care of the dispersiveness in B2B phase referencing in the submm regime, especially near the band edges higher than Band 6, where the relative dispersive term can reach  $\sim 50\%$ . We discuss our observing frequency selection in HF-LBC-2017, taking into account the dispersiveness, in Section 3.

Another concern is that ionospheric phase errors have an inverse quadratic dependence on the observing frequency and can be expanded using the  $R$  scaling ratio. One of the well-known ionospheric perturbations is nighttime periodic medium-scale traveling ionospheric disturbances (MSTIDs; e.g., Otsuka et al. 2013) with an amplitude of  $\sim 1$  TECU at most ( $1 \text{ TECU} = 10^{16} \text{ electron m}^{-2}$ ). Typically, MSTIDs typically have a horizontal wavelength of a few hundred km, so that the spatial irregularities in the longest ALMA baselines do not yield a significant error in the frequency-transferred phase. On the other hand, it has been reported that equatorial plasma bubbles with a horizontal size of a few hundred km are often observed in the early evening to midnight above the South America (e.g. Takahashi et al. 2016, 2018). They have a spatial gradient of  $0.1 - 0.2 \text{ TECU km}^{-1}$  at most, corresponding to a spatial TEC difference of  $\sim 2 \text{ TECU}$  at the longest ALMA baselines. Let us quantitatively evaluate the frequency-transferred phase error. Assuming the sources observed at the elevation angle of  $50^\circ$ , the worst case of  $\Delta TEC$  at the ALMA site can be  $2 \times \sec Z_i \text{ TECU}$ , where  $Z_i$  is the zenith angle of the sources for an altitude of 300 km (bottom of the ionospheric F-region). Considering  $\nu_{\text{HF}} = 873 \text{ GHz}$  and  $\nu_{\text{LF}} = 97 \text{ GHz}$  (the largest frequency separation possible for B2B phase referencing at ALMA; also see Section 2.5), the frequency-transferred phase error due to the plasma bubbles in Equation (4) is  $0.78 \text{ rad TECU}^{-1}$ . This leads to a frequency-transferred phase error of  $\sim 113^\circ$ , and it becomes one-ninth of this when using another possible  $\nu_{\text{LF}}$  solution of 291 GHz. The equatorial plasma bubbles are more frequently observed during southern hemisphere summer seasons, so that one may have to consider choosing a smaller  $R$  for observations conducted before midnight in summer seasons. Note that this error term can be mitigated by selecting a nearby DGC source later discussed in Section 2.2.

One note regarding B2B phase referencing is the instrumental phase offset difference that appears in the last term of Equation (4). The actual stabilities of the instrumental phase in ALMA satisfy the system-level requirements (Matsushita et al. 2012), so for in-band phase referencing, this term cancels out; however, it remains as a systematic phase error in B2B phase referencing. The correction of this phase error is discussed in the next section.

The term  $\tau_{\text{bl}}^{\text{T}}(t) - \overline{\tau_{\text{bl}}^{\text{C}}}(t)$  is dominated by an inner product of the baseline error vector and the separation angle vector between the target and phase calibrator. We assess how small the separation angle needs to be in order to mitigate this effect in this feasibility study.

The term  $\tau_{\text{trp}}^{\text{T}}(t) - \overline{\tau_{\text{trp}}^{\text{C}}}(t)$  is randomly variable due to the residual atmospheric phase fluctuations. Here we estimate the RMS of  $\tau_{\text{trp}}^{\text{T}}(t) - \overline{\tau_{\text{trp}}^{\text{C}}}(t)$ . This is considered to be proportional to the square root of the spatial structure function

for atmospheric phase fluctuations as a function of  $d + v_w t_{\text{swt}}/2$  for baselines whose length is longer than this value, where  $v_w$  is the velocity in meters per second of the atmosphere at the height of the turbulent layer, and  $d$  is the geometrical distance in meters between the lines of sight to the target and the phase calibrator at the altitude of the turbulent layer (Holdaway & D’Addario 2004). Assuming an atmospheric turbulent layer height of 500 m and its velocity of  $6 \text{ m s}^{-1}$  at the ALMA site (Robson et al. 2001), and that the phase calibrator is horizontally  $3^\circ$  separated from the target at the elevation angle of  $50^\circ$ ,  $d + v_w t_{\text{swt}}/2 = 34 + 3t_{\text{swt}}$ , so that the atmospheric phase fluctuation can be greatly reduced by selecting a short switching cycle time. Regardless of in-band or B2B phase referencing, the switching cycle time must be short enough (Matsushita et al. 2017) and the separation angle should be as small as possible in order to cancel out the phase errors from the baseline errors and atmospheric phase fluctuations.

In the case of B2B phase referencing, since the thermal noise in the calibrator phase is computationally frequency phase-transferred with  $R$  and applied to the target phase through the phase correction process, it is recommended to select a bright calibrator at  $\nu_{\text{LF}}$ , which still is much easier than finding a phase calibrator at  $\nu_{\text{HF}}$  as later discussed in Section 5.

## 2.2. DGC

By applying the frequency-transferred correcting phase as expressed in the last term of Equation (4), B2B phase referencing induces the instrumental phase offset difference. The instrumental phase offset difference can be independently measured with a cross-band calibration (Holdaway & D’Addario 2004) in which a quasar is observed at  $\nu_{\text{HF}}$  and  $\nu_{\text{LF}}$  in turn to obtain the phase difference. In this paper, this cross-band calibration block is referred to as DGC, such that the observed calibrator for this purpose is referred to as a DGC source. Figure 1 schematically shows a unit of DGC to obtain a solution, which is called the DGC block.

In the DGC block, the delay error due to the baseline error is canceled out by phase referencing between HF and frequency-transferred LF phases because this delay error is proportional to the inner product of the baseline vector error and the separation angle vector, while the separation angle is  $0^\circ$  in this case. Note that there could be a small delay error due to the uncertainty of the a priori source position, where the brightness peak for a DGC source may not be exactly consistent between  $\nu_{\text{HF}}$  and  $\nu_{\text{LF}}$  due to core shift properties of active galactic nuclei (Hada et al. 2011). The expected quantities are typically smaller than 0.1 mas, corresponding to a few tens of femtoseconds for a 16 km baseline, so that we can neglect this effect in the following discussion. The phase difference at time  $t$  can be expressed as follows:

$$\begin{aligned} \Delta\Phi^{\text{DGC}}(t) &= 2\pi\nu_{\text{HF}} \left[ \tau_{\text{trp}}^{\text{DGC}}(t) - \overline{\tau_{\text{trp}}^{\text{DGC}}}(t) \right] + \left[ \Phi_{\text{therm-H}}^{\text{DGC}}(t) - R \overline{\Phi_{\text{therm-L}}^{\text{DGC}}}(t) \right] \\ &+ \frac{2\pi\kappa}{c\nu_{\text{HF}}} \left[ \Delta\text{TEC}^{\text{DGC}}(t) - R^2 \overline{\Delta\text{TEC}^{\text{DGC}}}(t) \right] + \left[ \Phi_{\text{inst-H}}^{\text{DGC}}(t) - R \overline{\Phi_{\text{inst-L}}^{\text{DGC}}}(t) \right]. \end{aligned} \quad (5)$$

In Equation (5), the first and second terms are random variables. The RMS of the first term is proportional to the square root of the structure function as a function of  $v_w t_{\text{swt}}/2$  for baselines whose length is longer than this value, as discussed in Section 2.1. Therefore, the shorter the switching cycle time is for DGC, the smaller the atmospheric phase noise becomes in  $\Delta\Phi^{\text{DGC}}$ . The switching cycle time for the frequency switching is of the order of 20 – 30 s. In this case, the atmospheric phase fluctuations are tracked exceptionally well and calibrated by the frequency phase transfer. If we take a time average of equation (5) to suppress the random noise, we obtain the following phase error:

$$\langle \Delta\Phi^{\text{DGC}}(t) \rangle = \frac{2\pi\kappa(1-R^2)}{c\nu_{\text{HF}}} \langle \Delta\text{TEC}^{\text{DGC}} \rangle + \left\langle \Phi_{\text{inst-H}}^{\text{DGC}} - R \overline{\Phi_{\text{inst-L}}^{\text{DGC}}} \right\rangle. \quad (6)$$

The above phase solution preserves the ionospheric phase error directed to the DGC source and the instrumental phase offset difference between the HF target and LF phase calibrator. The first term is negligible for relatively small ionospheric perturbations, such as MSTIDs. Even in the case of a relatively large  $R$  and an enhanced ionospheric anomaly, the frequency-transferred ionospheric phase error can be canceled out between the target and DGC source by selecting a nearby DGC source (Dodson & Rioja 2009). At last, the DGC solution should be subtracted from Equation (4) to obtain fully calibrated target visibility data.

### 2.3. Implementation of B2B phase referencing and DGC

In the implementation of B2B phase referencing in the actual data reduction, we deal with the instrumental phase offsets at  $\nu_{\text{HF}}$  and  $\nu_{\text{LF}}$  separately, as depicted in a logical workflow in Figure 3. In Figure 3,  $\Phi_{\text{LF}}^{\text{DGC}}$ ,  $\Phi_{\text{HF}}^{\text{DGC}}$ ,  $\Phi_{\text{LF}}^{\text{C}}$ , and  $\Phi_{\text{HF}}^{\text{T}}$  are observed phases of the DGC source at  $\nu_{\text{LF}}$  and  $\nu_{\text{HF}}$ , phase calibrator at  $\nu_{\text{LF}}$ , and target at  $\nu_{\text{HF}}$ , respectively. In the workflow, a single interferometer signal output is assumed at each of  $\nu_{\text{HF}}$  and  $\nu_{\text{LF}}$ . The WVR phase correction and the system noise temperature correction have been applied to all of the data before this workflow starts. The bandpass calibration and flux scaling using a flux calibrator are done only for the HF phase and amplitude.

We derive a time-averaged solution for all of the LF DGC scans  $\langle \Phi_{\text{LF}}^{\text{DGC}} \rangle$  (panel (a) in Figure 3), that represents an LF phase offset for each antenna. In the next step, we apply  $\langle \Phi_{\text{LF}}^{\text{DGC}} \rangle$  to the LF DGC phases  $\Phi_{\text{LF}}^{\text{DGC}}$  and derive short-term phase solutions  $\Delta \Phi_{\text{LF}}^{\text{DGC}}$  for atmospheric phase fluctuations alone (free from other offsets) at each LF DGC scan (panel (b)). These solutions are frequency phase-transferred, and applied to the HF DGC phases  $\Phi_{\text{HF}}^{\text{DGC}}$  (panel (c)). This should correct the HF atmospheric fluctuations, so the HF DGC data can then be averaged in time and used to derive a HF phase offset  $\langle \bar{\Phi}_{\text{HF}}^{\text{DGC}} \rangle$  (panel (d)). We then apply the LF phase offset  $\langle \Phi_{\text{LF}}^{\text{DGC}} \rangle$  to the LF phase calibrator phase  $\Phi_{\text{LF}}^{\text{C}}$  to remove the common LF phase offset and to obtain the short term phase solutions  $\Delta \Phi_{\text{LF}}^{\text{C}}$  containing corrections for atmospheric fluctuations at  $\nu_{\text{LF}}$  for each LF phase calibrator scan (panel (e)). Finally, the HF phase offset correction  $\langle \bar{\Phi}_{\text{HF}}^{\text{DGC}} \rangle$  is applied to the target phase  $\Phi_{\text{HF}}^{\text{T}}$ , along with the time-dependent phase solutions derived from the LF phase calibrator,  $\Delta \Phi_{\text{LF}}^{\text{C}}$  (panel (f)). In this paper, we refer to the DGC HF phase offset  $\langle \bar{\Phi}_{\text{HF}}^{\text{DGC}} \rangle$  as the DGC solution for the sake of convenience.

### 2.4. Fast switching

In our feasibility study, we used fast switching with switching cycle times of 20 – 82 s. For almost all of the experiments, the scan length per source was 8 s; thus, accounting for a few seconds overhead for the antenna slew and/or frequency switching, the resulting switching cycle time was 20 s, considerably faster than the 100 s that is currently used for Cycle 7 user observations in Band 8 with a 3.6 km maximum baseline ( $B_{\text{max}}$ ) configuration in ALMA. We note that the image quality with longer switching cycle times can be investigated by culling phase calibrator scans (Maud, L. T. et al. in preparation).

In fast switching, a relative pointing difference of the 12 m antenna between two sources separated by less than  $2^\circ$  is about  $0.''6$ . In B2B phase referencing, pointing and focus adjustments between two Bands also have to be made by mechanically changing the position of the subreflector mounted on a 6-dimensional positioning actuator, as well as adjusting the relative pointing offset in the azimuth and elevation axes. The pointing offsets of the 12 m antenna between Bands are well maintained with an accuracy of  $2''$  or higher. The relative pointing offset, for instance, between Bands 7 and 9 can be determined with a typical deviation of  $0.''3$ – $0.''5$ . The 12 m antennas have a field of view of  $58''$  and  $9''$  in Bands 3 and 9, respectively.

### 2.5. Harmonic frequency switching

In the case that frequency switching observations like B2B phase referencing are made using ALMA without any consideration, a temporal overhead of  $\sim 20$  s takes place for every frequency switching event that requires a retuning of the photonic local oscillator (LO) signal (Shillue et al. 2012). This hinders the fast switching and essentially makes 20 s switching cycle times with frequency switching impossible. To minimize the overhead time and maximize reliability when using B2B phase referencing, we switch Bands using a fixed photonic LO frequency for both receivers; i.e., the photonic LO is tuned once at the start of an observation and not retuned in the repeated frequency switching. Each Band multiplies the photonic LO frequency with a small configurable offset of 20 – 45 MHz from an auxiliary oscillator in each antenna by a different fixed factor to obtain the actual first LO (LO1) frequency. The factor is referred to as a cold multiplier, as it is performed by a multiplier chain in the cold cartridge of the receiver. This technique is referred to as harmonic frequency switching and can minimize the overhead to  $\sim 2$  s.

Each Band can only be used over a particular photonic frequency range, so not all receivers available to ALMA can be paired at an arbitrary frequency. The possible band combinations in B2B phase referencing are listed in Table 1. We have to note that Bands 1 and 2 have not yet been implemented in ALMA. For completeness, Band 1 cannot form a harmonic frequency pair with any other Band, whereas Band 2 could pair with Bands 6, 8 and 9, the latter being most important for HF observations. There are some prohibited HF LO1 ranges, as listed in Table 2, for which no matching LF LO1 is available. In HF-LBC-2017, we adopted harmonic frequency switching for all of the B2B phase referencing experiments.

### 3. STRATEGY OF HF-LBC-2017

In HF-LBC-2017, we conducted a series of experiments in order to implement B2B phase referencing in ALMA step-by-step in the following four stages: (1) confirm that the ALMA observing system correctly executes a B2B phase referencing observation procedure as designed, (2) ensure that DGC solutions do not have unexpected temporal instabilities or sky position dependencies, (3) quantify the difference between B2B and in-band phase referencing in the image quality, and (4) verify that astronomical celestial sources can be imaged with a suitable image fidelity at HF using long baselines. In the campaign, we organized test observations in Bands 7, 8, 9, and 10 (285–875 GHz) with the baselines up to 16 km. We conducted two Band 10 experiments, one each for stages 2 and 3. Both failed after that because the observed sources were too weak to confirm whether the fringes were detected or not. In this paper, the Band 10 results are not mentioned further.

The stage 1 test began in early 2017 and lasted until June. During this stage, we confirmed that the ALMA observing system could correctly operate the B2B phase referencing sequence and that the antenna and/or frequency fast switching could work without major technical troubles. The stage-1 test is not mentioned further in this paper.

From 2017 March to July, we conducted the tests of stages 2 and 3 tests using the mid-baseline lengths ( $B_{\max} \sim 400$  m–4 km) to check the DGC solution stability and a basic image performance for various separation angles and switching cycle times. In stage 3, we compared the image quality between B2B and in-band phase referencing. One of the interesting parts of the study at stage 3 is the investigation of imaging performance between in-band and B2B phase referencing when the same phase calibrator is used, as well as when more distant calibrators are used for in-band phase referencing.

The baselines were longer than 10 km from the middle of July to the end of November, during which time more stage 3 tests and the stage 4 tests were undertaken. For stage 4, using the long baselines ( $B_{\max} \sim 14$ –16 km), we conducted high angular resolution imaging experiments to demonstrate science-like observations of a QSO in Bands 7 and 8 and initiated B2B phase referencing experiments for two complex structure sources, HL Tau and VY CMA, in Band 9. Tables 3–5 summarize the basic parameters of the experiments performed during stages 2, 3, and 4, respectively, together with the information of the ALMA execution blocks (EBs).

In selecting the observing frequencies, we prioritized the following two points: (1) the harmonic frequency switching is available for a combination of HF and LF to achieve the fast switching, and (2) the dispersive term due to the atmospheric water vapor is not very large to adopt a simple frequency scaling ratio ( $R = \nu_{\text{HF}}/\nu_{\text{LF}}$ ). The selected spectral regions used in HF-LBC-2017 are superimposed in Figure 2. Although spectral regions with a relatively large dispersive term were used in Bands 8 and 10, we adopted the simple frequency scaling ratio for B2B phase referencing because other comparable delay errors, such as the antenna position errors, do not have a frequency dependence. Optimization of the frequency scaling ratio for a given frequency combination must be a future subject for B2B phase referencing.

## 4. RESULTS

In this section, we discuss the main results from the experiments in stages 2–4. We adopted a consistent switching cycle time of  $\sim 20$  s, typically consisting of 8 s target and phase calibrator scans and two 2 s overheads to switch sources and/or frequencies. We note that the complex structure source imaging test in stage 4 had longer switching cycle times, described in Sections 4.3.2 and 4.3.3. The WVR phase correction was always applied through HF-LBC-2017. Throughout almost all of the tests, there were a number of manual flagging commands to be entered for these data, mostly for the frequency switching segments, due to the nature of testing such an experimental observation mode, though the problem was identified and fixed during stage 4. For many parts of our data reduction, we made use of the Common Astronomy Software Applications (CASA) package (McMullin et al. 2007).

### 4.1. Stage 2: DGC solution stability

We arranged two sets of experiments in stage 2: one set targeting several bright QSOs as DGC sources in succession with the sky separations of up to  $100^\circ$  to check the dependence of the DGC solutions with the sky position, and another targeting a single DGC source for over an hour to check the long-term stability. In this paper, we report the former stability test results. We organized the stage 2 test first from the compact configuration with  $B_{\max} = 400$  m in March to  $B_{\max} = 3$  km in June. Figure 4 shows examples of array configurations of the stage 2 test in 2017 April and May.



In the actual ALMA receivers, each Band amplifies two linear polarizations ( $X$  and  $Y$ ) separately, so that each polarized signal has an independent instrumental phase offset. The amplified signal is split into four intermediate-frequency signals which are called basebands (BBs) with a bandwidth of 2 GHz and an independent phase offset from each other. The BBs are digitized at the antenna and transferred to the correlator. In the correlator, the digitized BBs are filtered out to have a user-defined flexible bandwidth, frequency resolution, and polarization pairs among  $XX$ ,  $XY$ ,  $YY$ , and  $YX$  to form a spectral window (SPW) with a uniformly spaced spectral channels.

Figure 5 shows an example of one DGC block to observe a bright QSO (in this case, J2253+1608) and the data reduction procedure for the Band combination of 7 and 3 (Band 7–3) on 2017 April 11, as listed in Table 3. One DGC block basically consists of four HF and five LF scans. The LO1 frequencies in Bands 7 and 3 are 285 and 95 GHz, respectively. The top panel shows the WVR-corrected antenna-base phase of a baseline between two 12 m antennas (DV17 and DV09 in Figure 4) for the  $XX$  polarization pair. Phase offsets for an HF SPW (crosses) and LF SPW (open squares) were artificially adjusted to make them align each other (for plotting purposes). The middle panel is the same as the top panel, but the Band 3 phases are multiplied by the frequency scaling ratio. The bottom panel shows the Band 7 phases after correcting with the Band 3 phase and that the Band 7 phase time variation can be corrected using the Band 3 phases that are multiplied by the frequency scaling ratio. After the B2B phase referencing correction, the HF phase is averaged to one point, so that the time interval is  $\sim 90$  s for a single DGC solution in this case.

Figure 6 shows the results of the same experiment but for a total of five bright QSOs, four SPWs, and two polarization pairs ( $XX$  and  $YY$ ). The left panels plot the WVR-corrected antenna-based phases in Band 7 with respect to the reference antenna (DV09) before the phase correction, whereas the right panels plot the antenna-based DGC solution averaged at each DGC block. A simple mean for each SPW and each polarization pair was removed. In the left panels, there are large time variations, which can be stabilized after the phase correction, as shown in the right panels. Some antennas still show a common behavior in the corrected phase between the SPWs and the polarization pairs in the DGC solution. The randomness of the DGC solutions can be due to the residual atmospheric phase fluctuations as expressed in the first term of Equation (5). Considering how B2B phase referencing for a target will be implemented, such drifts, if occurring, can be calibrated by inserting the interpolated solutions determined from multiple DGC blocks in an observation. The DGC solution changes in the same way at each antenna for all of the SPWs and polarization pairs. This indicates that the randomness of the DGC solution is attributed not to the thermal noise but rather to the atmospheric phase fluctuations and/or the LO signal stability difference between the Bands.

Figure 7 is similar to Figure 6, but shows the DGC solutions of Band 8–4 (462–154 GHz) and Band 9–6 (675–225 GHz) conducted on 2017 May 4 and April 23, respectively. In Band 8–4, we observed four bright QSOs but analyzed two of them (J0510+1800 and J0522–3627; open triangles and open circles in the left panel, respectively) because the other two have antenna shadowing effects at around  $30^\circ$  elevations. In Band 9–6, we analyzed two of the five observed QSOs (J1924–2914 and J1517–2422; filled circles and crosses, respectively, in the right panel) because the other three do not have high enough S/Ns in Band 9. In those HF cases, the DGC solutions show not only a random phase behavior but also a linear trend more or less with approximately a few degree per minute at maximum as represented with the dotted lines in the left panels. These linear trends may be caused by instrumental instabilities that are under investigation.

Figure 8 shows the antenna-based DGC solutions as a function of baseline length to the reference antenna after subtracting a single linear trend for each antenna. The DGC solution in Band 7 has a roughly a standard deviation of  $10^\circ$ – $20^\circ$ , independent of the sky positions of the QSOs. We note that 200 m baselines have a larger deviation than 20 m baselines. This is thought to be because of the residual atmospheric phase fluctuations. As discussed in Section 2.2, the deviation of the DGC solution can increase until a baseline length of  $v_w t_{\text{swt}}/2$ . If we assume  $v_w = 6 \text{ m s}^{-1}$ , this baseline length is expected to 60 m.

Figure 9 is similar to Figure 8, but in Bands 8–4 and 9–6. The DGC solutions at those HFs are also independent of sky position; however, the standard deviation of the DGC solution is increased to  $\sim 30^\circ$ . Comparing with the Band 7–3 result, those higher-frequency experiments show higher phase instability mainly because of the residual atmospheric phase fluctuations and instrumental phase instabilities at the observing frequency. Some antennas have a large deviation between the SPWs and/or show that the LF and HF phases do not track each other; thus, the DGC solution is more variable, indicating instrumental malfunctions or instabilities, generating a more variable DGC solution. Such issues led to investigation of antenna components that were then serviced or replaced.

From the stage 2 test, we found that the DGC is satisfactorily stable, i.e. there are no rapid instrumental variations, excluding obvious problematic antennas. As a whole, the DGC solutions are stable for QSOs with positions separated by  $100^\circ$  apart on the sky. For future B2B phase referencing observations, the DGC block will be executed two or three times in an observation to provide ample calibration of the instrumental phase offset difference and linear trend.

The stabilities of the DGC solutions were also investigated in stages 3 and 4. In stage 3, a DGC source was observed at the start and end of an observation, separated by around 40–45 minutes; in stage 4, a DGC source was repeatedly observed every 15 minutes during 1–2 hr. In the stage 2 test, we reconfirmed that, except for some problematic antennas showing phase drifts, the RMS phase noise of the DGC solutions is typically  $10^\circ$ – $20^\circ$  in Band 7, while this can increase to  $30^\circ$ – $40^\circ$  in Bands 8 and 9. Generally, as part of the later-stage feasibility checks with a baseline out to 16 km, the instrumental phase offset difference determined from the DGC solution is stable for approximately 1 hr.

#### 4.2. Stage 3: image quality comparative test between B2B and in-band phase referencing

Comparative studies of the HF image quality between B2B and in-band phase referencing falls into two categories: (1) the same target and the same phase calibrator are used for both B2B and in-band phase referencing, and (2) B2B phase referencing uses a small separation of  $1^\circ$ – $2^\circ$ , and in-band phase referencing uses a larger separation (typically  $3^\circ$ – $11^\circ$ ). The specific goals of this comparative study are summarized as follows: (1) confirm that B2B and in-band phase referencing produce the same result when using the same phase calibrator and (2) indicate whether B2B phase referencing is an improvement over in-band phase referencing if using a closer phase calibrator, as per the intended use of B2B phase referencing. In typical observations, the separation to phase calibrators is usually larger at higher frequencies due to the difficulties in finding a bright enough source (see Section 5 for more details). We tried to mimic such a situation in stage 3.

A series of the stage 3 experiments started in 2017 July and were performed in a variety of weather conditions (atmospheric phase stability) and with a range of total number of antennas (typically  $> 20$ ). Various harmonic frequency pairs were tested (Bands 7–3, 8–4, 9–4, 9–6, and 10–7). A single experiment was formed by the combination of the B2B and in-band phase referencing blocks, as well as two DGC blocks executed in the following sequence: (DGC)—(in-band phase referencing)—(B2B phase referencing)—(in-band phase referencing)—(B2B phase referencing)—(DGC). In the above sequence, the same target was observed for both the B2B and in-band phase referencing blocks, whereas different phase calibrators were used for each phase referencing block. The total length of each observing block was  $\sim 8$  minutes, including a system noise temperature measurement and pointing calibration. The full run of the sequence takes 45–50 minutes.

The data reduction of the in-band phase referencing was undertaken with a standard ALMA data reduction procedure, while the B2B phase referencing data reduction procedure requires the application of the DGC solutions. For the amplitude calibration, we used the DGC source as an HF flux calibrator in addition to the system noise temperature calibration in both the B2B and in-band phase referencing. For the imaging, we use a Briggs weighting with a robustness parameter (robust) of 0.5, as this is representative of the common robust generally used in ALMA images. A fixed number of 50 CLEAN iterations were made with a 15 pixel radius masking box around the target (located at the phase tracking center in the image). The cell size is chosen such that 5 (for Bands 7 and 8) or 7 (Band 9) pixels cover the synthesized beam major axis. Due to the nature of the experiment sequence, we can cull phase calibrator scans in order to mimic longer switching cycle times to investigate any potential relationships between the image quality, switching cycle time, and weather condition.

The full study of 50 datasets will be detailed in the forthcoming paper (Maud, L. T. et al. in preparation). In this paper, we detail only one of the Band 8–4 experiments that is unique in having four observing sequences run together on the same night, comparing four different phase calibrator separation angles for the in-band phase referencing. The LO1 frequencies were 400 and 133 GHz for the target and phase calibrator, respectively, in the case of B2B phase referencing. Figure 10 shows a subset of three out of the four Band 8 images from the consecutive experiments on 2017 July 18 targeting QSO J0633–2333 using B2B (left) and in-band (right) phase referencing with the switching cycle time of 60 s obtained by culling phase calibrator scans. We selected four phase calibrators, J0634–2335, J0620–2515, J0648–1744, and J0609–1542, located at separation angles of  $1.^\circ 2$ ,  $3.^\circ 8$ ,  $5.^\circ 8$ , and  $8.^\circ 7$  from the target, respectively. The B2B phase referencing was tested only to the closest calibrator, J0634–2335, while in-band phase referencing was tested to all four. The synthesized beam sizes are 80–100 mas. The execution pair with the  $3.^\circ 8$  in-band phase referencing failed because the sources eventually transited close to zenith, so that more than half of the data had to be flagged out, and the resultant image quality was poor.

In order to check the image quality after phase referencing, we performed phase self-calibration (Schwab 1980) with a short solution interval (here we could use a solution interval of  $\sim 1$  s as the S/N was high) and obtained images free from the residual atmospheric and instrumental phase errors. Here we define the image coherence as the ratio between peak flux densities for data with and without self-calibration applied. The higher the image coherence is, the more effective phase referencing we achieve, and the highest image coherence is 1. The top row images of Figure 10 indicates that the peak flux densities are almost identical for B2B and in-band phase referencing—that is, the image coherence is almost unity—and that the image structure is pointlike with few defects, although the B2B phase referencing image noise is higher. The increased image noise is due to inaccuracies in the DGC. After self-calibration, the image noise of the B2B and in-band phase referencing are equivalent, indeed confirming that the residual offsets have been fully corrected. In the middle and bottom rows of Figure 10, when the in-band phase calibrators are located further away, the image coherence and image dynamic range begin to decrease, and the level of defects increases. Since the target image with the  $1.^\circ 2$  phase calibrator in B2B phase referencing remains largely unchanged, this degradation in the image quality is considered to be attributed to the larger separation angles. Assuming that the residual RMS phase noise in the visibility has characteristics of a Gaussian random noise, the image coherence can be equivalent to a coherence factor  $\exp(-\sigma_\phi^2/2)$ , where  $\sigma_\phi$  is the residual RMS phase noise in radians (Thompson et al. 2001). Note, importantly, that the atmospheric phase fluctuations over the switching cycle time are low ( $< 35^\circ$ ), and therefore the conditions are stable and should allow all images to achieve  $>85\%$  image coherence.

Figure 11 compiles the above Band 8–4 experiment. The left panel summarizes the peak flux densities of the target images in Figure 10 as a function of the separation angle, clearly showing the decrease in peak flux with increasing separation angle. Relative to the image obtained for the closest phase calibrator, the peak flux density falls below 80% for the images with the  $5.^\circ 8$  and  $8.^\circ 7$  separation angles. Relative to the self-calibrated image, the image coherence is 71% and 64% for the  $5.^\circ 8$  and  $8.^\circ 7$  separation angles.

The right panel of Figure 11 shows the offset of the image peak positions from the a priori phase tracking center of the target. The imaging result has a positional uncertainty of 10 – 20% of the synthesized beam size for a separation angle of up to  $8.^\circ 7$ , although the image with the  $8.^\circ 7$  in-band phase calibrator becomes more distorted than the others with the closer phase calibrators. Considering the image coherence and defects, the phase calibrator in this case should be located closer than  $5^\circ$ – $6^\circ$ .

Taking into account all the sets of comparative experiments, the image coherence of B2B phase referencing is comparable to that of in-band phase referencing when using the same close phase calibrator, although naturally in-band phase referencing is marginally better considering the additional DGC required for B2B phase referencing. On the other hand, we found that in-band phase referencing has a noticeable degradation of image quality in terms of the image coherence and defects with increasing separation angle. Specifically, for the longest baseline test data, where  $\nu_{\text{HF}} < 300$  GHz and maximal baselines were 15 km in stage 3, provided the atmospheric stability is good (over the switching cycle time), in order to obtain an image coherence  $\geq 70\%$  the phase calibrator separation angle should be within  $\sim 6^\circ$ . Although we have not systematically tested the B2B phase referencing image quality for a variety of separation angles, the tendency is expected to be the same as the image quality with in-band phase referencing if using more distant phase calibrators. Since B2B phase referencing requires the additional DGC, our findings of the separation angle dependency of in-band phase referencing are applicable as an upper limit of the image quality of B2B phase referencing.

For higher frequencies than 400 GHz, although we have small number statistics and the baseline lengths are shorter,  $< 5$  km, the degradation seems to be respectively worse; i.e., it is a function of frequency and baseline length. This makes sense as the worse calibration causing a reduced coherence are due to delay errors related to underlying uncertainties in antenna positions (Hunter et al. 2016), and are frequency dependent when converted to phase. For higher frequencies, it is likely that calibrators even closer than  $6^\circ$  would be required for the longer baseline.

#### 4.3. Stage 4: high angular resolution imaging test

In order to investigate the feasibility of high angular resolution imaging with extended array configurations at high frequencies, ALMA quasi end-to-end observation experiments were arranged in stage 4. Here we present Band 7–3 and Band 8–4 experiments of a point source (QSO), and Band 9–4 experiments of two extended sources (HL Tau and VY CMa) that have complex structures. In stage 4, we experimentally applied a  $90^\circ$  phase switching in the correlator (Thompson et al. 2001) in Band 9, so that the bandwidth of the HL Tau and VY CMa observations was doubled, compared to that of normal science observations in Cycle 5.

Figure 12 shows the array configuration of the stage-4 test on 2017 Nov 3. The longest and shortest baseline lengths are 13.8 km and 133 m, corresponding to angular resolutions of 7 mas and 0.7 arcsec in Band 9, respectively. Note, there were only a few baselines shorter than 200 m during the stage-4 period and thus we could not properly sample structures larger than 0.2 arcsec. The observed target sources, phase calibrators and DGC sources of the experiments are listed in Table 5.

#### 4.3.1. Point-source target: QSO J2228–0753 in Bands 7–3 and 8–4

The QSO J2228–0753 was observed as a continuum point-source target in Bands 7 and 8, while QSO J2229–0832, with a separation angle of  $0.7^\circ$ , was observed as a phase calibrator at an LF. We selected a bright QSO, J2253+1608, as a DGC source located  $25^\circ$  away from the target. The high LO1 frequencies are 289 (Band 7) and 405 (Band 8) GHz, while the corresponding low LO1 frequencies are 96 (Band 3) and 135 (Band 4) GHz, respectively. Array configurations with  $B_{\max} \sim 14 - 16$  km were arranged containing 40–50 12-m antennas. The observations were carried out using standard science scheduling blocks (Nyman et al. 2010). We used a 20 s switching cycle time for B2B phase referencing between the target and phase calibrator, as well as for the frequency switching cycle on the DGC source. The on-source scan length at the HFs was 8 s. The left and right panels of Figure 13 show the synthesized images in Bands 7 and 8, respectively, using a Briggs robust 0.5 weighting in CASA CLEAN when combining two EBs taken in the middle of October and the beginning of 2017 November. The achieved beam sizes are  $19 \times 16$  and  $16 \times 12$  mas in Bands 7 and 8, respectively. Further details of the observations and data analysis results are described in another paper (Asaki et al. 2019).

We also performed phase self-calibration with a solution interval of the target scan length and obtained the images free from the atmospheric and instrumental phase errors in order to investigate the image coherence. We obtained high image coherences of 94% and 84% in Bands 7 and 8, respectively, so that B2B phase referencing works effectively in those experiments. We note that there are cases in imaging where a Briggs robust of  $> 0.5$  or, in extreme cases, a natural weighing with an addition taper are required to notably increase the beam size ( $> 50\%$ ) and the sensitivity to larger angular scales in order to mitigate resolving out a source with considerable extended structures. In these QSO observations, it does not matter if one adopts a robust of 0.5 because the observed QSO is a point source even with the above angular resolutions. The 94% image coherence in Band 7 corresponds to an RMS phase noise of  $21^\circ$ , and the Band 8 image coherence of 84% is consistent with an RMS phase noise of  $34^\circ$ .

#### 4.3.2. Complex structure target I: HL Tau in Band 9–4

Located in the Taurus molecular cloud, HL Tau is a protoplanetary disk system surrounding a young star at a distance of 140 pc (Rebull et al. 2004). This system is very young, and its age is estimated to be less than 1 Myr (Beckwith et al. 1990; Robitaille et al. 2007). It is the first of two complex structure sources observed to examine whether the image quality of B2B phase referencing is as expected in Band 9 when compared with the known high-fidelity image from previous ALMA SV data. The SV observations of HL Tau show substructures of bright rings and dark gaps in the disk in Bands 3, 6, and 7, which strongly indicate the presence of protoplanets (ALMA Partnership et al. 2015b).

Two B2B phase referencing EBs were taken on 2017 November 3 with switching cycle times of 37 and 26 s, respectively. The scan lengths obtained for HL Tau were 27 and 16 s, while a 6 s scan was obtained on a phase calibrator, QSO J0431+1731,  $0.7^\circ$  away from HL Tau. The total observing time was 65 and 100 minutes for the first and second executions, respectively. Combined, there is 45 minutes on-source time for HL Tau. The DGC source QSO J0522–3627 is  $56^\circ$  away from the target and was repeated twice in the first EB and three times in the second. The LO1 frequencies for the target and the phase calibrator are 671 (Band 9) and 149 (Band 4) GHz, respectively. The correlator was configured to have eight SPWs in Band 9 with a bandwidth of 2 GHz each using the  $90^\circ$  phase switching. The PWV was 0.53 mm. Due to instrumental instabilities, a number of flags were applied so that some of the longest baseline antennas were flagged out; thus, we could not achieve the expected  $\sim 10$  mas angular resolution with the EBs. We evaluated the image fidelity of our Band 9 data by comparison with the long baseline SV in Band 7 in LBC-2014 (ADS/JAO.ALMA #2011.0.00015.SV, hereafter LBC-2014-SV).

Figure 14 presents the HF-LBC-2017 images of HL Tau in Band 9 after combining the two EBs. For the left and middle images, natural and Briggs (robust = 0.5) weightings are used, as Briggs weightings with smaller robustness parameters form too-sharp beams resolving out almost all of the extended emission. The final beams achieved were  $20 \times 18$  and  $14 \times 11$  mas, respectively. Using the high-S/N bandpass calibrator observation, we performed an assessment of the Band 9 RMS phase with a time interval of 30 s, slightly longer than the switching cycle time of the first EB. The

RMS phase was still considerably high around  $50^\circ$ ; thus, the atmosphere was at the stability limit for Band 9 when already accounting for the very short switching cycle time. Under the assumption that phase referencing corrects all timescales longer than a half of the switching cycle time, we would expect an image coherence of up to 65%–70%. Using the simple assumption that the central peak of emission is completely optically thick ( $\alpha=2$ ), scaling from the LBC-2014-SV Band 7 data ( $11.56 \text{ mJy beam}^{-1}$ , ALMA Partnership et al. 2015b), the estimated peak flux density at 671 GHz would be expected to be  $\sim 44 \text{ mJy beam}^{-1}$ . The naturally weighted HF-LBC-2017 Band 9 image yields a peak of  $24.9 \text{ mJy beam}^{-1}$ , suggesting a coherence of around 56%. We have not, however, performed any form of self-calibration and note that the beam is slightly smaller compared to the LBC-2014-SV image; hence, this is likely the lower limit of the coherence.

In our Band 9 image, a few clear features related to the bright and dark lanes in the disk can be discerned. Measured along the major axis, at a radius of  $\sim 0.''09$  (13 au), we see a strong depression of emission, while at  $\sim 0.''13$  (19 au), there is a slight increase in flux. The features are coincident with D1 and B1, dark and bright features reported by ALMA Partnership et al. (2015b). The next dark region at  $\sim 0.''22$  (31 au) related to feature D2 is only partially visible in the naturally weighted image when contrasted against the somewhat brighter feature to the southeast at  $\sim 0.''26$  (37 au) that is an arc shape representing the incomplete B2 ring. The Briggs-weighted image resolves out any larger scales. However, we have to mention that a simple comparison is not exactly fair because the total on-source time is 45 minutes and we have not performed any self-calibration, whereas in ALMA Partnership et al. (2015b), the images are comprised of 10 EBs with 5 hr on-source time, and self-calibration was performed. Furthermore, due to the relatively short on-source time and the handful of short baselines, the poor  $(u, v)$  sampling of the largely extended disk structure causes a striped side-lobe pattern throughout our Band 9 image at the 50%–60% level with natural weighting. Spatially the side lobe is roughly colocated with the bright large ring B6; however, its structure is far from complete. Natural weighting is not the optimal choice; however, the robust 0.5 Briggs weighting already begins to resolve the disk bright and dark substructures. Similarly, the right panels of Figure 14 are after reimaging but excluding the short baselines  $< 500 \text{ k}\lambda$  ( $\sim 220 \text{ m}$  in Band 9 sensitive to scales  $> 0.''5$ ) and using a natural weighting. Some of the side lobes are alleviated, but again, the disk substructures start to be resolved out.

To provide a fairer comparison of the image structure, we use only one Band 9 HF-LBC-2017 EB compared with a Band 7 image with a single LBC-2014-SV EB. We used the second execution of the HF-LBC-2017 data with the shorter switching cycle time and longer on-source time (26 minutes). Comparatively, there was a similar on-source time for each single execution of the LBC-2014-SV data (30 minutes), although HF-LBC-2017 has twice the bandwidth using the  $90^\circ$  phase switching. The LBC-2014-SV Band 7 image using the full  $(u, v)$  range is shown in the top right panel of Figure 15. A robust of  $-1$  was used for the LBC-2014-SV data to push toward higher angular resolutions and provide a better match with the HF-LBC-2017 angular resolution. The resultant synthesized beam size is  $24 \times 10 \text{ mas}$ . The equivalent B2B phase referencing image in Band 9 is shown on the top left, which has a beam of  $20 \times 18 \text{ mas}$ . In the single EB for the LBC-2014-SV data, the ringlike structure in the central  $0.''3\text{--}0.''4$  is reasonably evident, whereas in HF-LBC-2017, the image striping dominates the eye, again due to using natural weighting to still be sensitive to the disk bright and dark substructures. For further comparison, when limiting the  $(u, v)$  range of the LBC-2014-SV (and also changing to robust=0.5 to keep the beam reasonably matched to the B2B phase referencing image) and HF-LBC-2017 data the resultant images are more similar, as shown in the bottom left and right panels of Figure 15, respectively, because as expected, both resolve out the majority of the extended structure. Aside from the unfortunate  $(u, v)$  sampling, based upon these fairer comparisons, our Band 9 image of HL Tau is arguably as good as that in Band 7.

#### 4.3.3. Complex structure target II: VY CMa in Band 9–4

Our second high-resolution imaging experiment targeted VY CMa, located at a distance of 1.17 kpc (Zhang et al. 2012). It is an oxygen-rich red supergiant (RSG) with a variable but exceptionally high mass-loss rate. The high mass-loss rate (up to  $10^{-3} M_\odot \text{ yr}^{-1}$ ) provides bright spectral line and continuum emissions within a few arcseconds, making it one of the best targets for the image fidelity check by comparison with the previous SV in Band 9 in LBC-2013 with a  $B_{\text{max}}$  of 2.7 km (ADS/JAO.ALMA #2011.0.00011.SV, hereafter LBC-2013-SV) not only for the continuum emission but also for the  $658.00655 \text{ GHz } v_2 = 1, 1_{1,0} - 1_{0,1} \text{ H}_2\text{O}$  maser (Richards et al. 2014).

On 2017 November 3, VY CMa was observed in Band 9 with a switching cycle time of 82 s. The scan lengths for VY CMa and the phase calibrator QSO J0725–260, at  $1.^\circ 1$  away from VY CMa, were 62 and 12 s, respectively. The total observing time was 47 minutes, and the on-source time for VY CMa was 344 s. The PWV was 0.56 mm. The

LO1 frequencies for the target and the phase calibrator are 669 (Band 9) and 149 (Band 4) GHz, respectively. The correlator was configured to have eight SPWs in Band 9 with a bandwidth of 1.875 GHz each using the  $90^\circ$  phase switching. One of the SPWs covers the 658 GHz  $\text{H}_2\text{O}$  maser with the frequency resolution of 15.625 kHz. A bright QSO, J0522–3627,  $28^\circ$  away from the target, was used as the DGC source, as well as for bandpass and flux-scale calibration.

The line-free continuum emission image using the averaged eight SPWs with Briggs weighting (robust = 2) is shown in the left panel of Figure 16. The synthesized beam size is  $12 \times 11$  mas, and the image RMS noise is  $1.5 \text{ mJy beam}^{-1}$ . In the initial map, there is a bright and compact component (VY CMa) that cannot be resolved even with the longest baselines, so that the self-calibration can be applied to the data (such a compact component is ideal for performing self-calibration). In order to obtain the visibility data free from the atmospheric and instrumental phase errors, phase and amplitude self-calibrations were performed for the line-free continuum channels with the solution interval of 16 s to remove residual phase offsets between the SPWs. The self-calibration solutions were then applied to all target data, and the bright maser peak, which has a higher S/N, was used for further self-calibration, now making and applying the solutions with an interval of 4 s to all data. Improvements were seen on the continuum peak, which increased from 42 to  $135 \text{ mJy beam}^{-1}$ , while the image RMS noise was largely unchanged at  $1.5 \text{ mJy beam}^{-1}$ . This indicates that stochastic phase errors remained even after B2B phase referencing, which gave an image coherence loss of  $\sim 70\%$ . The rather long switching cycle time in Band 9 may cause a significant coherence loss due to the atmosphere. Using the high-S/N bandpass calibrator observation (after applying WVR corrections only), we performed an assessment of the Band 9 RMS phase with a time interval of 40 s, approximately a half of the switching cycle. The RMS phase was extremely high for all of our Band 9 observations around  $80^\circ$ , corresponding to a coherence loss of 62%. It is expected that a shorter switching cycle time would have been better for the atmospheric phase fluctuation condition, although due to the nature of these tests, the observations were performed during available time and thus not during the most optimal conditions. The final self-calibrated image with the eight SPWs' line-free emission is shown in the middle panel of Figure 16.

The right panel of Figure 16 shows the LBC-2013-SV continuum image for comparison with the synthesized beam size of  $110 \times 59$  mas. It is observed in the LBC-2013-SV image that extended, cooler dust from the northern plume (N plume) and eastern clump (C clump) are prominent, while VY CMa cannot be clearly resolved due to heavy dust obscuration and the larger synthesized beam size. The diffuse C clump can still be detected with our high angular resolution. This indicates that there are complex substructures in this dust emission, while the N plume is almost resolved out. Those resolved emissions probably contribute to the slightly high continuum RMS of  $1.4 \text{ mJy beam}^{-1}$  while a  $0.7\text{--}1.0 \text{ mJy beam}^{-1}$  noise level is predicted across the line-free continuum, depending on the reference frequency.

Our self-calibrated image shows that VY CMa can be resolved almost into a point source with minor diffuse emission along the same direction as the N Plume. O’Gorman et al. (2015) estimated a stellar contribution of 111–124 mJy at around 658 GHz based on the analytical stellar properties. The HF-LBC-2017 resolution has enabled us to resolve the star with at most  $\sim 10 - 20\%$  contribution from dust. A resolved two-dimensional Gaussian component fitted to VY CMa in the LBC-2013-SV image (right panel of Figure 16) gave a flux density of 358 mJy in an area of  $146 \times 74$  mas after deconvolving the beam. Fitting to a similar sized-aperture for VY CMa in our image gives 394 mJy at the reference frequency of 669 GHz. These results are consistent within the  $\sim 20\%$  error for the LBC-2013-SV fluxes.

It is expected that the unresolved point source in HF-LBC-2017 represents the RSG photosphere with the diameter of 11.4 mas (Wittkowski et al. 2012). The peak position of VY CMa was estimated before the self-calibration to be located at  $(\alpha, \delta) = (7^{\text{h}}22^{\text{m}}58^{\text{s}}.3261, -25^\circ46'03''.038)$  (J2000). The position is offset by (47, 5) mas from the position measured from the most astrometrically accurate LBC-2013-SV observations at 321 GHz in Band 7 (resolution of  $180 \times 90$  mas). The LBC-2013-SV positional uncertainty is 35 mas, and the shift is likely to be affected also by the contribution of the extended dust emission in the larger LBC-2013-SV beam in Band 7. As discussed in Section 4.2, the peak offset is expected to be 10–20% of the synthesized beam size at most using a phase calibrator within  $5\text{--}6^\circ$ . We are still investigating this positional offset to understand whether it is intrinsic due to the annual parallax and proper motion (Zhang et al. 2012), and/or instrumental interferometer phase errors.

A bright submm  $\text{H}_2\text{O}$  maser cube with a velocity resolution of  $8 \text{ km s}^{-1}$  was generated for the 18 averaged frequency channels as shown in Figure 17. For the  $\text{H}_2\text{O}$  maser cube, we applied Briggs weighting (robust = 0.5) to achieve a higher angular resolution because astronomical maser emissions are thought to be very compact (typically 1 au, or 0.9 mas at a distance of 1.17 kpc), so that the maser emission is compact even with a narrower synthesized beam:

the resultant synthesized beam size is  $10 \times 8$  mas. For comparison, the continuum emission map is superposed on the  $\text{H}_2\text{O}$  maser cube. The continuum image was made with Briggs weighting ( $\text{robust} = 0$ ) to compare relative positions between the photosphere emission and maser cloud emission. The continuum emission map has a synthesized beam of  $10 \times 8$  mas and the image RMS noise of  $1.8 \text{ mJy beam}^{-1}$ . Since  $\text{H}_2\text{O}$  masers surrounding evolved stars are highly variable in general, we cannot identify which maser emissions correspond to those observed by Richards et al. (2014), but it is likely that groups of  $\text{H}_2\text{O}$  masers (maser features) surround the RSG as has been observed in the LB-2013-SV  $\text{H}_2\text{O}$  maser spot map.

## 5. DISCUSSIONS

We have technically proved the effectiveness of B2B phase referencing in HF long baseline observations at ALMA, and thus a final question arises: is B2B phase referencing more beneficial for selecting a phase calibrator than in-band phase referencing? Since the required flux density for a phase calibrator in B2B phase referencing is a factor of the frequency scaling ratio higher than that for in-band phase referencing as expressed in equation (3), the increase in the phase calibrator flux density and the antenna sensitivity at lower frequencies may not compensate for the low availability of phase calibrators at higher frequencies, especially with the largest frequency scaling ratio of Band 10–3 in the harmonic frequency switching.

To answer this question, we conducted calibrator source counts for B2B and in-band phase referencing using the ALMA calibrator source catalog.<sup>1</sup> In the catalog, 3316 QSOs whose flux densities have been measured with ALMA are available. In our analysis, flux density at an arbitrary frequency is evaluated by fitting the flux density measurements between Bands 3 and 7 or Bands 3 and 6 to a power-law function of  $\nu^\alpha$ , where  $\alpha$  is a spectral index. If a certain calibrator has been observed at multiple epochs, we refer to the highest value in order to list all possible sources that could be used as a phase calibrator.

The ALMA calibrator sources are not evenly distributed in the sky. For example, sources are more crowded along the Galactic plane, especially to the inner Galaxy. This is not because the calibrator sources are intrinsically more distributed in the Galactic plane but rather because more intensive surveys have been organized based on user-proposed targets. On the other hand, the flux density limited phase calibrator candidates in our investigation are the top 30% brightest sources in the catalog and are rather homogeneously distributed. We conclude that the current investigation is not seriously affected by the calibrator distribution bias. We constrain the decl. range lower than  $+25^\circ$ .

The basic parameters to calculate a flux density requirement for a phase calibrator are listed in Table 6. The system equivalent flux density (SEFD), which is flux density equivalent to the system noise temperature of the 12 m antenna (Thompson et al. 2001), is used for sensitivity calculation. The antennas are assumed to be directed to zenith. The available total bandwidth is 7.5 GHz in Bands 3–8 assuming that four 1.75 GHz SPWs are used, while in Bands 9 and 10, the total bandwidth is 15 GHz by configuring eight SPWs using the  $90^\circ$  phase switching in the correlator. The phase calibrator scan length is fixed to 8 s. First, we count only the sources whose flux density is higher than the flux density requirement. Second, we obtain a mean solid angle per phase calibrator from the above number count. Finally, we evaluate a mean angular separation to find a suitable phase calibrator in each Band.

The flux density requirement for the phase calibrator and the mean angular separation are listed in Tables 7 and 8 for B2B and in-band phase referencing, respectively. The phase calibrator availability in B2B phase referencing is superior to in-band phase referencing in Bands 8, 9, and 10. In Band 7, on the other hand, the availability is almost comparable between B2B and in-band phase referencing, so that there may not be a great merit in using B2B phase referencing. Band 10 is the most difficult Band in searching for an in-band phase calibrator, whose expected mean separation angle is  $12.^\circ6$ . By introducing B2B phase referencing, one is expected to find a suitable phase calibrator within  $4.^\circ3$  in Band 3. As discussed in Section 4.2, a phase calibrator would be required to be located within  $\sim 6^\circ$ , regardless of in-band and B2B phase referencing. The present investigation shows that B2B phase referencing is promising in searching for a closely located phase calibrator.

## 6. SUMMARY

The HF long baseline image capabilities of ALMA were successfully demonstrated by HF-LBC-2017 in Bands 7, 8, and 9 with B2B phase referencing when using switching cycle times of 20–82 s. The DGC solution shows no significant

<sup>1</sup> <https://almascience.nrao.edu/alma-data/calibrator-catalogue>

phase instability and is successfully applied to the target phase after B2B phase referencing to remove the instrumental phase offset difference.

We compared the image quality between B2B and in-band phase referencing by observing QSOs with various separation angles and with a range of weather conditions. In principle, the closer the separation angle to the phase calibrator, the better image quality we can obtain in both B2B and in-band phase referencing. The image coherence of B2B phase referencing with a 1–2° phase calibrator is comparable to that of in-band phase referencing with the same separation angle. It is considered that for larger separation angles, the image quality is degraded regardless of B2B and in-band phase referencing. If we wish to obtain an image coherence of  $\geq 70\%$ , the separation angle should be within  $\sim 6^\circ$ .

Our statistical investigation for the phase calibrator availability shows that B2B phase referencing is more beneficial for finding a phase calibrator in Bands 8–10 while there is no apparent merit in Band 7. These results demonstrate that the use of a closer phase calibrator together with B2B phase referencing can improve the image quality compared with in-band phase referencing in Bands 8–10.

We have conducted the imaging capability test using B2B phase referencing for QSO J2228–0753 in Bands 7–3 and 8–4, and for of HL Tau and VY CMa in Band 9–4. We successfully imaged those objects with the highest angular resolutions that can be achieved at each frequency with an image fidelity expected from previous ALMA observations. However, it is apparent for the complex structure sources that the visibility data cannot fully recover the extended structure without short  $(u, v)$  coverage. In the case of HL Tau, comparing to the previous Band 7 SV image, we sampled even smaller angular scales with the same baseline lengths in Band 9; thus, the image defects due to the undersampling of shorter  $(u, v)$  coverages are more clearly seen. Our results highlight that, for high-fidelity images of extended sources, it is essential to consider the combination of multiple array configurations to acquire shorter  $(u, v)$  coverages for achieving not only a detectable sensitivity but also well-sampled spatial frequency components.

The basic functionality of B2B phase referencing has been proven in HF-LBC-2017. On the other hand, there were several technical problems in the experiments, for example, more flagged raw data comparing with the ordinal ALMA observations and some problematic antennas showing a relatively large phase drift in the DGC solution in some cases. Another important subject not fully investigated for HFs is where the dispersive term of the atmospheric water vapor is greater than a few tens of percent. Solving these issue will be the goal of the next HF observational campaign.

For this research, we used the ALMA data listed in Tables 3–5, in addition to ADS/JAO.ALMA #2011.0.00015.SV and (HL Tau in Band 7) ADS/JAO.ALMA #2011.0.00011.SV (VY CMa in Band 9). This research made use of the online ALMA calibrator catalog

(<https://almascience.nrao.edu/alma-data/calibrator-catalogue>). ALMA is a partnership of ESO (representing its member states), NSF (USA), NINS (Japan), together with the NRC (Canada), NSC and ASIAA (Taiwan), and KASI (Republic of Korea), in cooperation with the Republic of Chile. The Joint ALMA Observatory is operated by the ESO, AUI/NRAO, and NAOJ. The authors thank the Joint ALMA Observatory staff in Chile for performing the challenging HF-LBC-2017 successfully. L. T. M. was adopted as a JAO ALMA expert visitor during his stay. This work was supported by JSPS KAKENHI grant No. JP16K05306.

*Software:* AATM (Nikolic 2009), CASA (McMullin et al. 2007)

## REFERENCES

- ALMA Partnership, Fomalont, E. B., Vlahakis, C., et al. 2015a, ApJL, 808, L1, doi: [10.1088/2041-8205/808/1/L1](https://doi.org/10.1088/2041-8205/808/1/L1)
- ALMA Partnership, Brogan, C. L., Pérez, L. M., et al. 2015b, ApJL, 808, L3, doi: [10.1088/2041-8205/808/1/L3](https://doi.org/10.1088/2041-8205/808/1/L3)
- ALMA Partnership, Vlahakis, C., Hunter, T. R., et al. 2015c, ApJL, 808, L4, doi: [10.1088/2041-8205/808/1/L4](https://doi.org/10.1088/2041-8205/808/1/L4)
- ALMA Partnership, Hunter, T. R., Kneissl, R., et al. 2015d, ApJL, 808, L2, doi: [10.1088/2041-8205/808/1/L2](https://doi.org/10.1088/2041-8205/808/1/L2)
- Andrews, S. M., Wilner, D. J., Zhu, Z., et al. 2016, ApJL, 820, L40, doi: [10.3847/2041-8205/820/2/L40](https://doi.org/10.3847/2041-8205/820/2/L40)
- Asaki, Y., Matsushita, S., Kawabe, R., et al. 2014, 2014SPIE 9145, 91454K, doi: [10.1117/12.2055824](https://doi.org/10.1117/12.2055824)
- Asaki, Y., Shibata, K. M., Kawabe, R., et al. 1998, RaSc, 33, 1297, doi: [10.1029/98RS01607](https://doi.org/10.1029/98RS01607)
- Asaki, Y., Sudou, H., Kono, Y., et al. 2007, PASJ, 59, 397, doi: [10.1093/pasj/59.2.397](https://doi.org/10.1093/pasj/59.2.397)
- Asaki, Y., Matsushita, S., Fomalont, E. B., et al. 2016, 2016SPIE 9906, 99065U, doi: [10.1117/12.2232301](https://doi.org/10.1117/12.2232301)
- Asaki, Y., Maud, L. T., Fomalont, E. B., et al. 2019, ApJ



- Bachiller, R., & Cernicharo, R. E. 2008, *Science with the Atacama Large Millimeter Array: A New Era for Astrophysics*, Berlin Heidelberg New York: Springer, Dordrecht
- Beasley, A. J., & Conway, J. E. 1995, *1995ASPC* 82, 82, 327
- Beckwith, S. V. W., Sargent, A. I., Chini, R. S., & Guesten, R. 1990, *AJ*, 99, 924, doi: [10.1086/115385](https://doi.org/10.1086/115385)
- Bryerton, E., Saini, K., Morgan, M., et al. 2005, in *The Joint 30th International Conference on Infrared and Millimeter Waves and 13th International Conference on Terahertz Electronics*, Vol. 1, 72–73
- Cliche, J. F., & Shillue, B. 2006, *IEEE Control Systems Magazine*, 26, 19, doi: [10.1109/MCS.2006.1580149](https://doi.org/10.1109/MCS.2006.1580149)
- Dodson, R., & Rioja, M. J. 2009, arXiv e-prints, arXiv:0910.1159. <https://arxiv.org/abs/0910.1159>
- Dodson, R., Rioja, M. J., Jung, T.-H., et al. 2014, *AJ*, 148, 97, doi: [10.1088/0004-6256/148/5/97](https://doi.org/10.1088/0004-6256/148/5/97)
- Hada, K., Doi, A., Kino, M., et al. 2011, *Natur*, 477, 185, doi: [10.1038/nature10387](https://doi.org/10.1038/nature10387)
- Han, S.-T., Lee, J.-W., Kang, J., et al. 2013, *PASP*, 125, 539, doi: [10.1086/671125](https://doi.org/10.1086/671125)
- Holdaway, M. A., & D’Addario, L. 2004, ALMA Memo 523. <http://library.nrao.edu/alma.shtml>
- Hunter, T. R., Lucas, R., Broguière, D., et al. 2016, *2016SPIE* 9914, 99142L, doi: [10.1117/12.2232585](https://doi.org/10.1117/12.2232585)
- Kervella, P., Homan, W., Richards, A. M. S., et al. 2016, *A&A*, 596, A92, doi: [10.1051/0004-6361/201629877](https://doi.org/10.1051/0004-6361/201629877)
- Matsushita, S., Asaki, Y., Kawabe, R., et al. 2014, *2014SPIE* 9145, 91453I, doi: [10.1117/12.2056424](https://doi.org/10.1117/12.2056424)
- Matsushita, S., Morita, K.-I., Barkarts, D., et al. 2012, *2012SPIE* 8444, 84443E, doi: [10.1117/12.925872](https://doi.org/10.1117/12.925872)
- Matsushita, S., Asaki, Y., Fomalont, E. B., et al. 2016, *2016SPIE* 9906, 99064X, doi: [10.1117/12.2231846](https://doi.org/10.1117/12.2231846)
- Matsushita, S., Asaki, Y., Fomalont, E. B., et al. 2017, *PASP*, 129, 035004, doi: [10.1088/1538-3873/aa5787](https://doi.org/10.1088/1538-3873/aa5787)
- Maud, L. T., Tilanus, R. P. J., van Kempen, T. A., et al. 2017, *A&A*, 605, A121, doi: [10.1051/0004-6361/201731197](https://doi.org/10.1051/0004-6361/201731197)
- Maud, L. T. et al. in preparation
- McMullin, J. P., Waters, B., Schiebel, D., Young, W., & Golap, K. 2007, *2007ASPC* 376, 376, 127
- Nikolic, B. 2009, ALMA Memo 587. <http://library.nrao.edu/alma.shtml>
- Nikolic, B., Bolton, R. C., Graves, S. F., Hills, R. E., & Richer, J. S. 2013, *A&A*, 552, A104, doi: [10.1051/0004-6361/201220987](https://doi.org/10.1051/0004-6361/201220987)
- Nyman, L.-Å., Andreani, P., Hibbard, J., & Okumura, S. K. 2010, *2010SPIE* 7737, 77370G, doi: [10.1117/12.858023](https://doi.org/10.1117/12.858023)
- O’Gorman, E., Vlemmings, W., Richards, A. M. S., et al. 2015, *A&A*, 573, L1, doi: [10.1051/0004-6361/201425101](https://doi.org/10.1051/0004-6361/201425101)
- Otsuka, Y., Suzuki, K., Nakagawa, S., et al. 2013, *AnGeo*, 31, 163, doi: [10.5194/angeo-31-163-2013](https://doi.org/10.5194/angeo-31-163-2013)
- Pardo, J. R., Cernicharo, J., & Serabyn, E. 2001, *ITAP*, 49, 1683, doi: [10.1109/8.982447](https://doi.org/10.1109/8.982447)
- Pérez, L. M., Lamb, J. W., Woody, D. P., et al. 2010, *ApJ*, 724, 493, doi: [10.1088/0004-637X/724/1/493](https://doi.org/10.1088/0004-637X/724/1/493)
- Rebull, L. M., Wolff, S. C., & Strom, S. E. 2004, *AJ*, 127, 1029, doi: [10.1086/380931](https://doi.org/10.1086/380931)
- Richards, A. M. S., Impellizzeri, C. M. V., Humphreys, E. M., et al. 2014, *A&A*, 572, L9, doi: [10.1051/0004-6361/201425024](https://doi.org/10.1051/0004-6361/201425024)
- Rioja, M. J., Dodson, R., Jung, T., et al. 2014, *AJ*, 148, 84, doi: [10.1088/0004-6256/148/5/84](https://doi.org/10.1088/0004-6256/148/5/84)
- Robitaille, T. P., Whitney, B. A., Indebetouw, R., & Wood, K. 2007, *ApJS*, 169, 328, doi: [10.1086/512039](https://doi.org/10.1086/512039)
- Robson, Y., Hills, R., Richer, J., et al. 2001, ALMA Memo 345. <http://library.nrao.edu/alma.shtml>
- Schwab, F. R. 1980, *SPIE*1980 231, 958828, doi: [10.1117/12.958828](https://doi.org/10.1117/12.958828)
- Shillue, B., Grammer, W., Jacques, C., et al. 2012, *2012SPIE* 8452, 845216, doi: [10.1117/12.927174](https://doi.org/10.1117/12.927174)
- Takahashi, H., Wrasse, C. M., Figueiredo, C. A. O. B., et al. 2018, *PEPS*, 5, 32, doi: [10.1186/s40645-018-0189-2](https://doi.org/10.1186/s40645-018-0189-2)
- Takahashi, H., Wrasse, C. M., Denardini, C. M., et al. 2016, *SpWea*, 14, 937, doi: [10.1002/2016SW001474](https://doi.org/10.1002/2016SW001474)
- Thompson, A. R., Moran, J. M., & Swenson, George W., J. 2001, *Interferometry and Synthesis in Radio Astronomy*, 2nd Edition (A Wiley-Interscience Publication, John Wiley & Sons, Inc.)
- Wittkowski, M., Hauschildt, P. H., Arroyo-Torres, B., & Marcaide, J. M. 2012, *A&A*, 540, L12, doi: [10.1051/0004-6361/201219126](https://doi.org/10.1051/0004-6361/201219126)
- Zauderer, B. A., Bolatto, A. D., Vogel, S. N., et al. 2016, *AJ*, 151, 18, doi: [10.3847/0004-6256/151/1/18](https://doi.org/10.3847/0004-6256/151/1/18)
- Zhang, B., Reid, M. J., Menten, K. M., & Zheng, X. W. 2012, *ApJ*, 744, 23, doi: [10.1088/0004-637X/744/1/23](https://doi.org/10.1088/0004-637X/744/1/23)

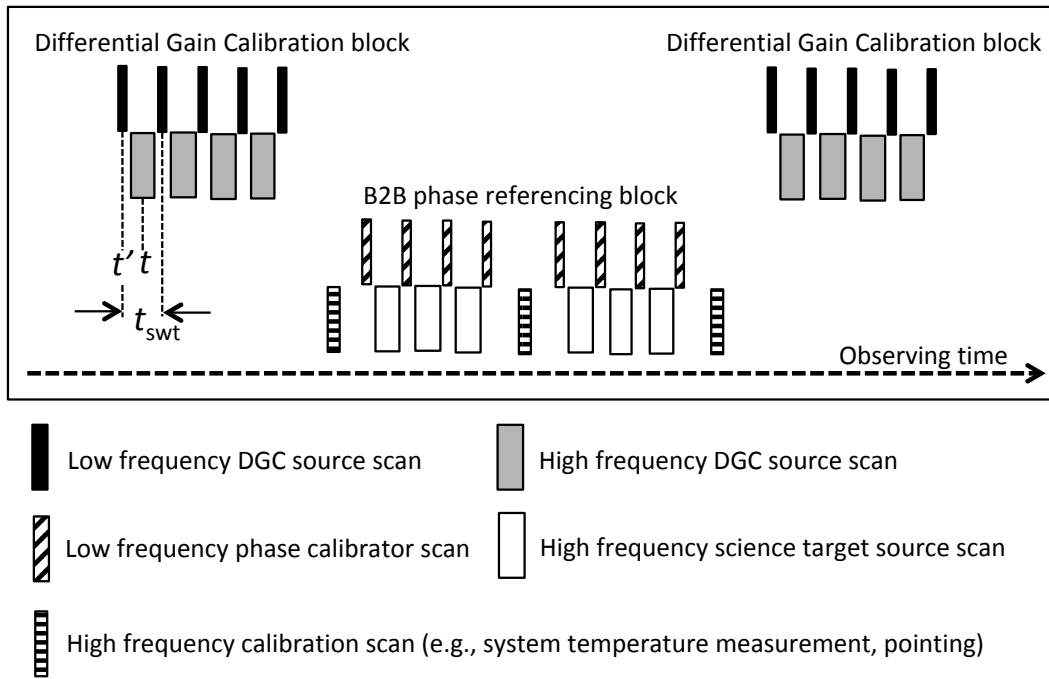


**Figure 1.** Typical sequence of a B2B phase referencing observation.

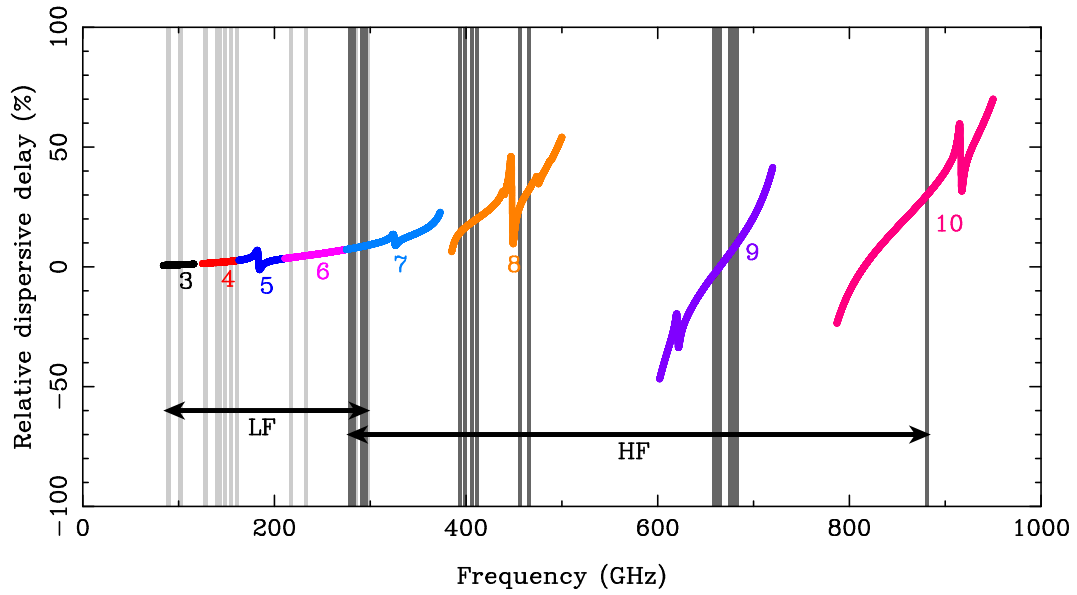


**Figure 2.** Relative dispersive delay of the atmospheric water vapor at the ALMA site ( $PWV = 1$  mm). The horizontal axis is the observing frequency, and the vertical axis is the relative dispersive delay compared to the nondispersive delay calculated with the ALMA ATM program (Nikolic 2009). The numbers in the plot represent the ALMA receiver bands. The light grey stripes in Bands 3–7 represent the LF spectra of the phase calibrators in HF-LBC-2017, while the dark grey ones in Bands 7–10 represent the HF spectra for the targets.

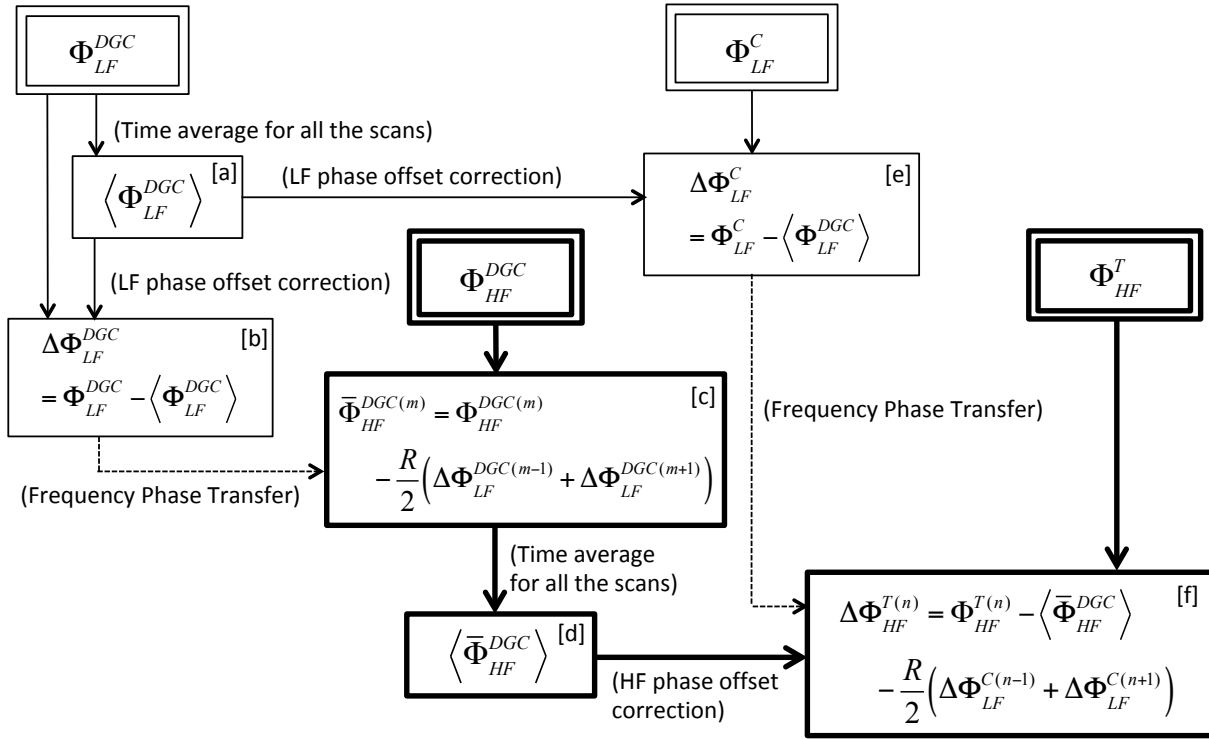


**Figure 3.** Logical workflow for implementation of B2B phase referencing and DGC. here  $\Phi_{LF}^{DGC}$ ,  $\Phi_{HF}^{DGC}$ ,  $\Phi_{LF}^C$ , and  $\Phi_{HF}^T$  surrounded by the double squares are observed phases of a DGC source at  $\nu_{LF}$  and  $\nu_{HF}$ , phase calibrator at  $\nu_{LF}$ , and target at  $\nu_{HF}$ , respectively;  $R$  is the frequency scaling ratio between  $\nu_{HF}$  and  $\nu_{LF}$ ; and  $n$  and  $m$  are arbitrary scan numbers. The dashed arrows represent frequency phase-transfer. The bold squares and arrows represent the HF data.

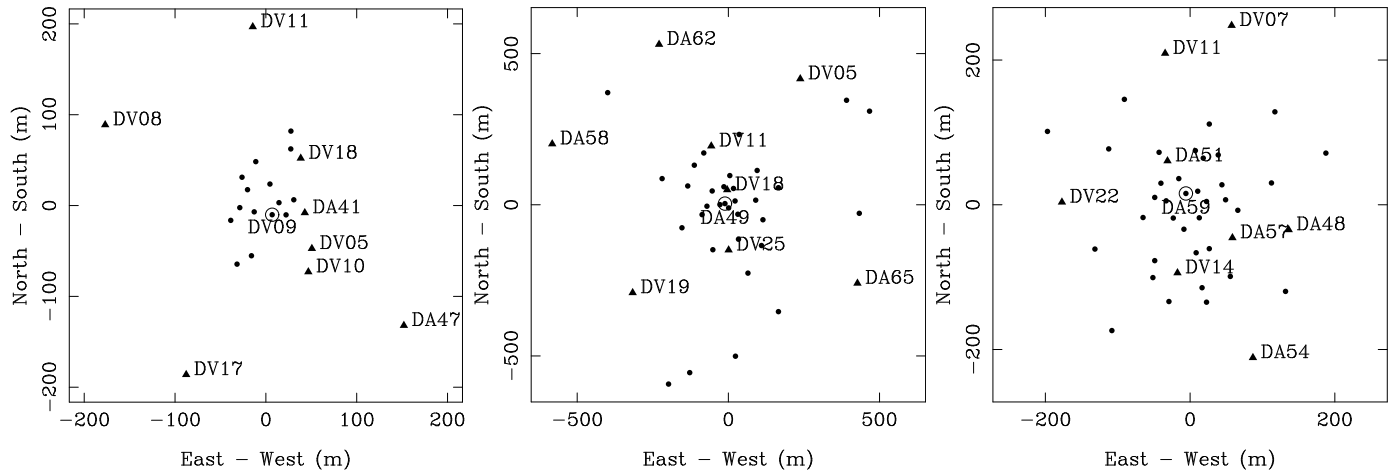


**Figure 4.** Array configurations of the stage 2 test. Left: Band 7–3 experiment on 2017 April 11. Filled symbols are antennas used in the experiment. The double circle represents the reference antenna (DV09) used for the antenna-based DGC solutions. The DGC solutions are shown in Figure 6 for antennas marked with triangles. Middle: Band 8–4 experiment on 2017 May 4. Right: Band 9–6 experiment on 2017 April 23. The DGC solutions of the Band 8–4 and 9–6 experiments are shown in Figure 7 for antennas marked with triangles.

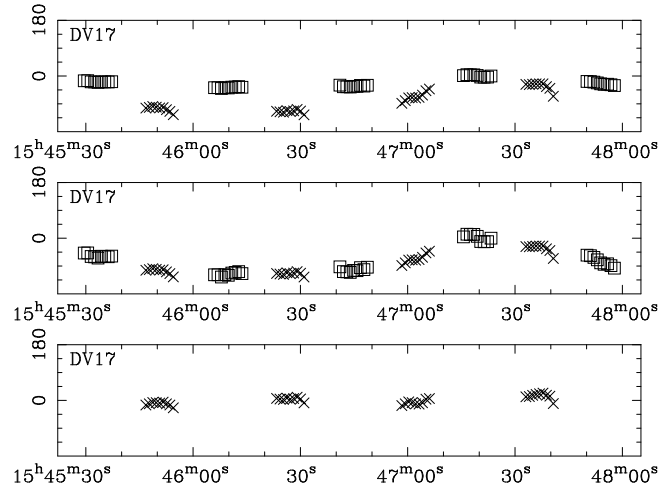


**Figure 5.** Stage 2 DGC stability experiment for Band 7–3 on 2017 April 11. Top: time series of the WVR-corrected antenna-based phase of J2253+1608 of the DV17 antenna for a single SPW with the  $XX$  polarization pair. Each point has a 1 s integration time. Crosses and open squares represent the Band 7 and Band 3 interferometer phases, respectively. Middle: the same as the top panel, but the Band 3 phases are multiplied by the frequency scaling ratio. Bottom: the Band 7 interferometer phases after correcting with the Band 3 phase time series, which are multiplied by the frequency scaling ratio.

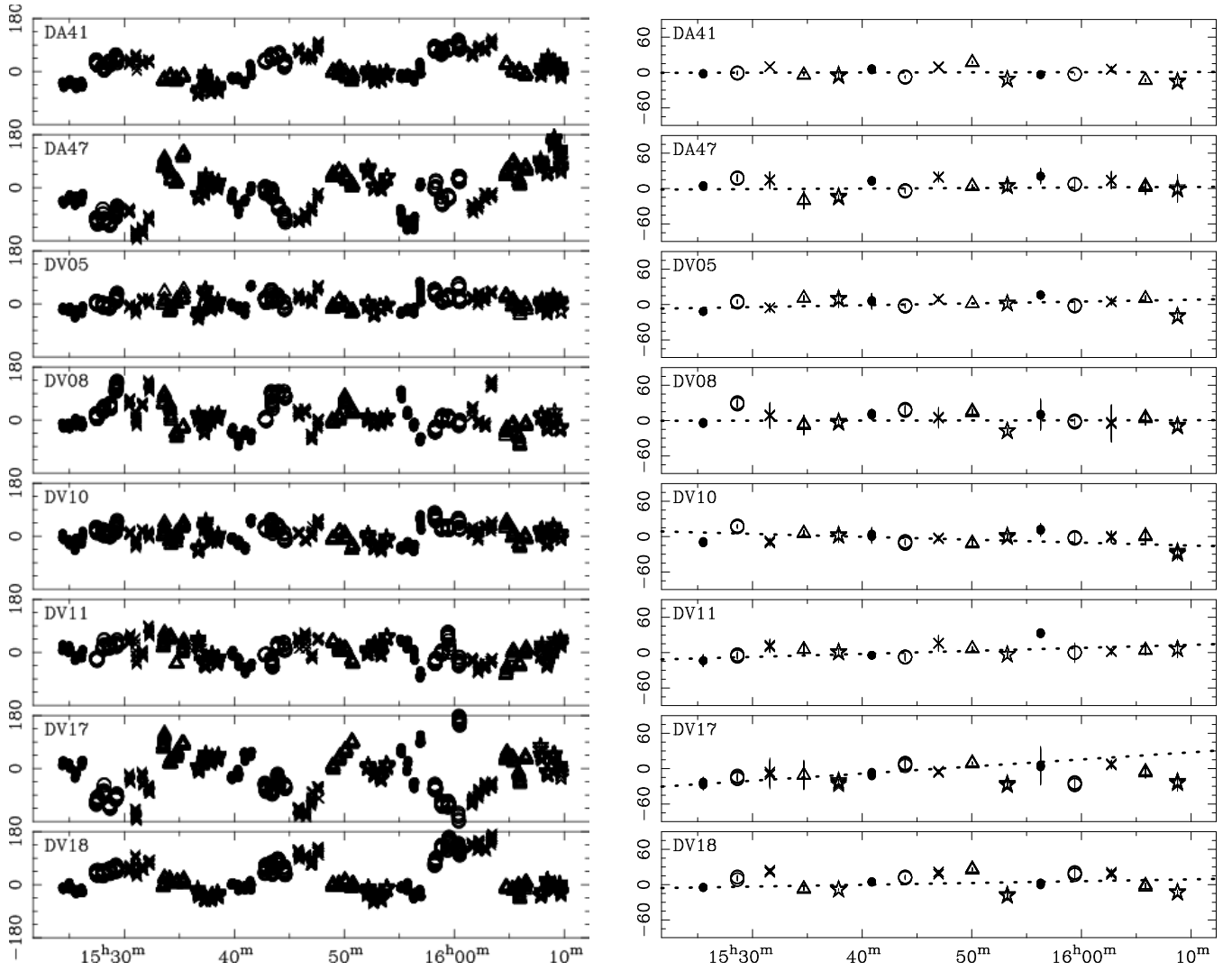


**Figure 6.** Stage 2 DGC stability experiment for Band 7–3 on 2017 April 11. Left: time series of the WVR-corrected antenna-based phase in Band 7 of J0006–0623, J2232+1143, J2253+1608, J0108+0135, and J2348–1631 (filled circles, open circles, crosses, open triangles, and open stars, respectively) after subtracting a mean phase per SPW per polarization pair ( $XX$  and  $YY$ ). Each symbol represents an 8 s scan-averaged phase for each SPW. Right: antenna-based DGC solutions per SPW per polarization pair. The time series are shown after subtracting a mean per SPW per polarization pair. The dotted line in each panel shows a linear fit to the phase residuals for each antenna.

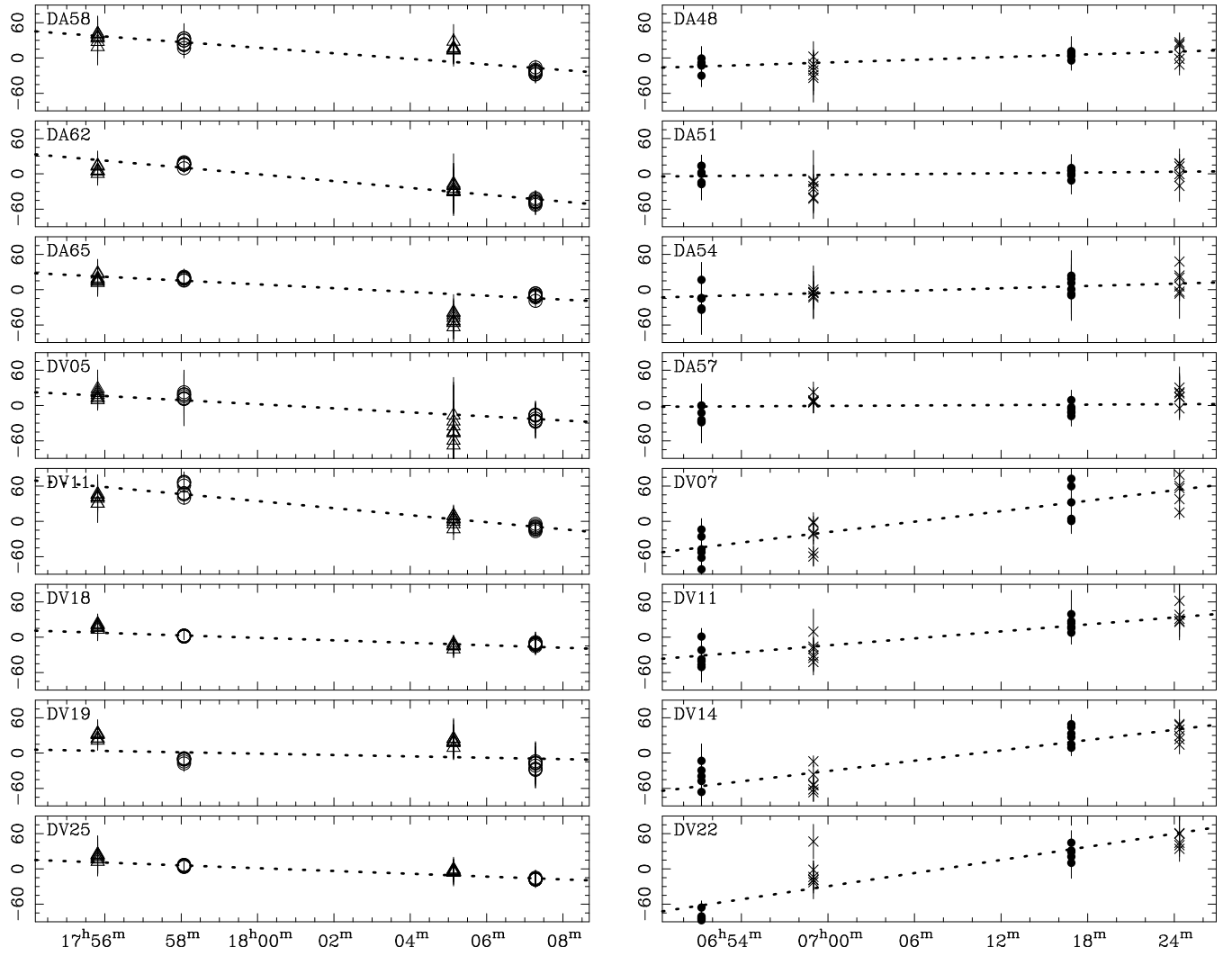


**Figure 7.** Stage 2 DGC stability experiments for Bands 8–4 (left) and 9–6 (right) on 2017 May 4 and April 23, respectively. The dotted line in each panel shows a linear fit to the phase residuals for each antenna. Left: in Band 8, two of the four observed QSOs are plotted (J0510+1800 and J0522–3627; open triangles and open circles, respectively). Right: in Band 9, two of the five observed QSOs are plotted (J1924–2914 and J1517–2422; filled circles and crosses, respectively).



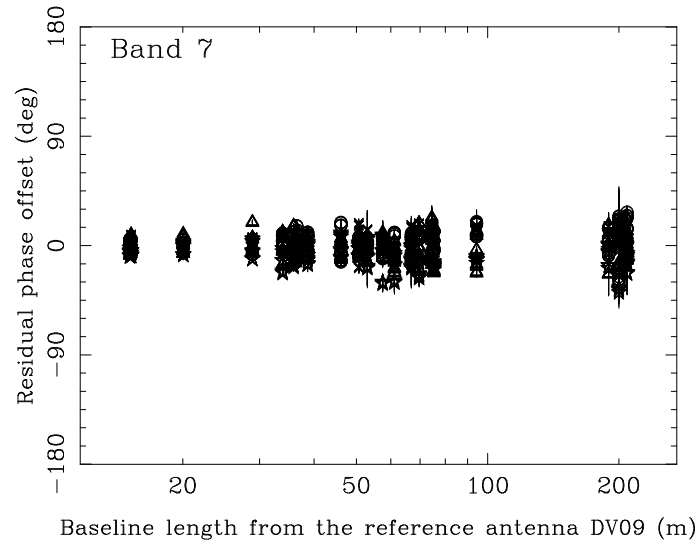


**Figure 8.** The DGC solution residuals of the stage 2 experiment in Band 7-3 (2017 April 11) for all the antennas and SPWs after subtracting the linear fit as represented by the dotted lines in Figure 6. The horizontal axis is the antenna distance with respect to the reference antenna. The vertical axis is the residual DGC solution after subtracting the linear fit.

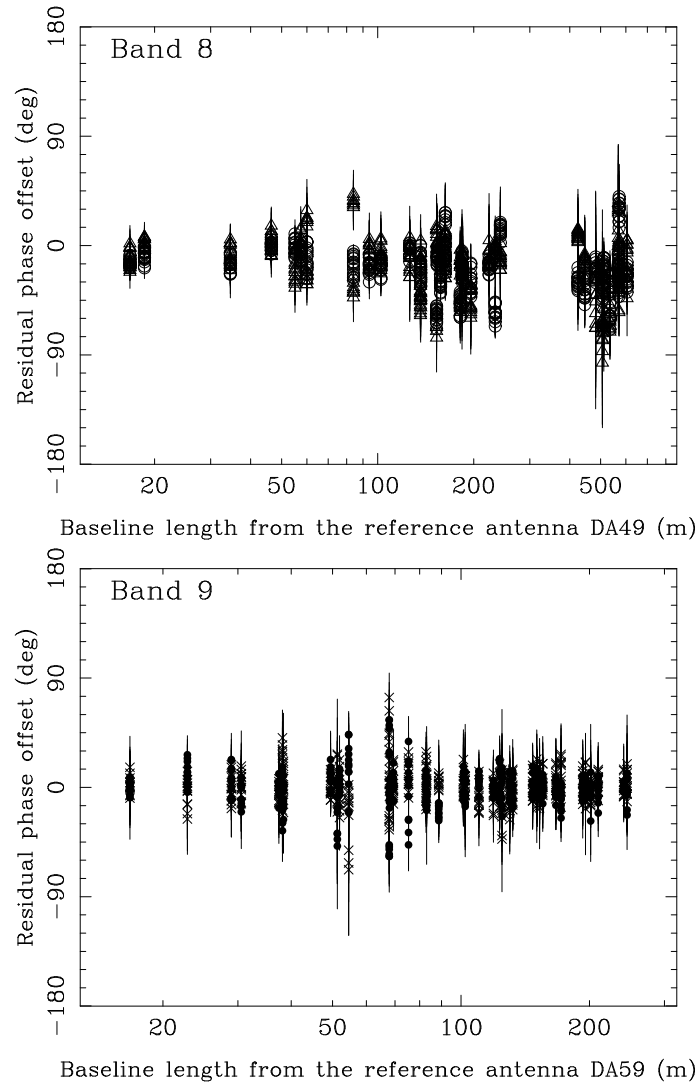


**Figure 9.** Same as Figure 8 but in Band 8–4 (2017 May 4) and Band 9–6 (2017 April 23) in the top and bottom panels, respectively.

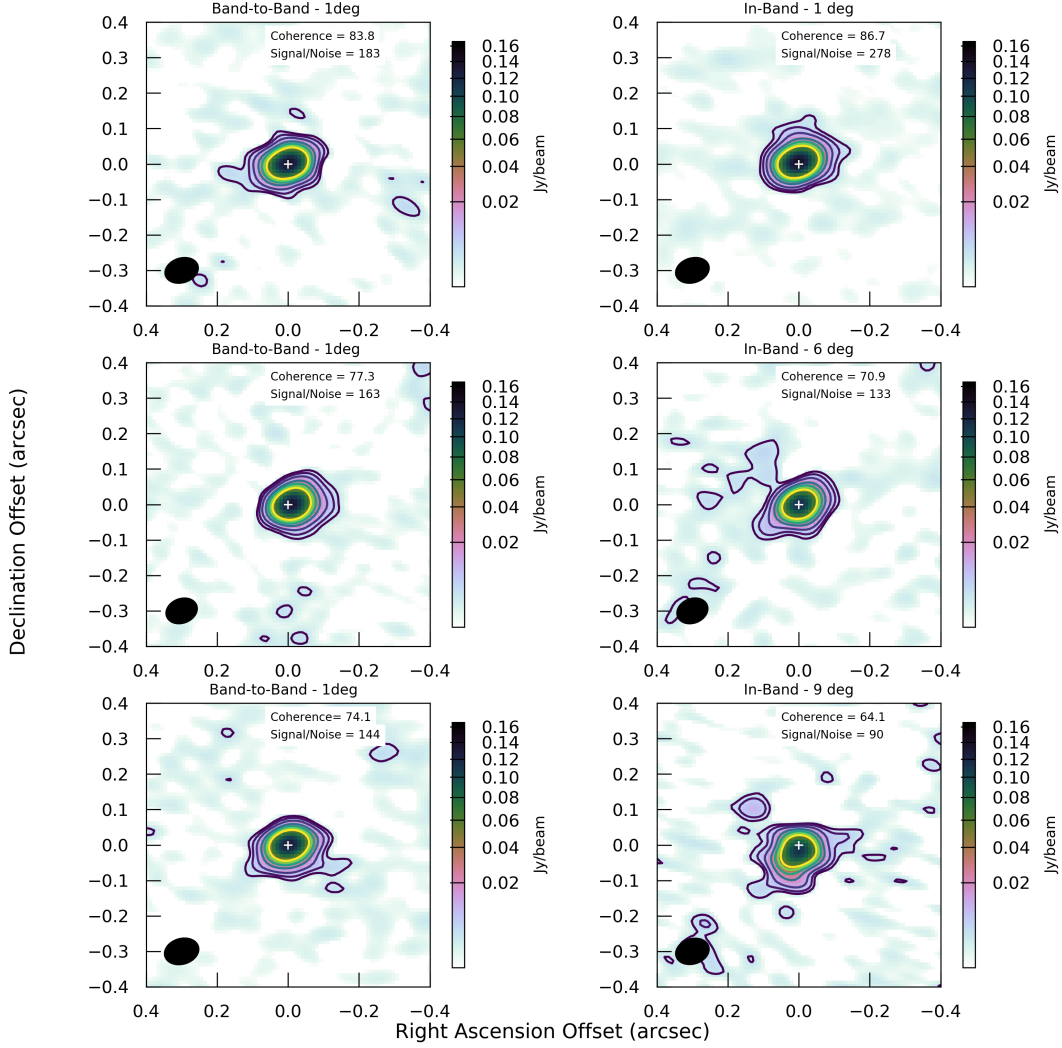


**Figure 10.** Synthesized images of J0633–2223 in Band 8 of the comparative experiment between B2B and in-band phase referencing on 2017 July 18 with a  $B_{\max}$  of 3.7 km. Each horizontal pair represents one experiment. Each row shows a consecutive execution pair and thus has similar weather conditions. The left panels show the B2B phase referencing images, where J0634–2335 at  $1.^{\circ}2$  was used as the phase calibrator. The paired in-band phase referencing images are shown in the right panels for the same target where phase calibrators of J0634–2335 ( $1.^{\circ}2$ ), J0648–1744 ( $5.^{\circ}8$ ), and J0609–1542 ( $8.^{\circ}7$ ) were used in the top, middle, and bottom panels, respectively. The images are all scaled to a flux peak of  $0.166 \text{ Jy beam}^{-1}$ , and the colored contours (dark to light) are fixed at 2.5, 5, 10, 20, 30, 40, and 50  $\text{mJy beam}^{-1}$  to highlight the image structure. Note that the image coherence is given in percent in the top of each panel.

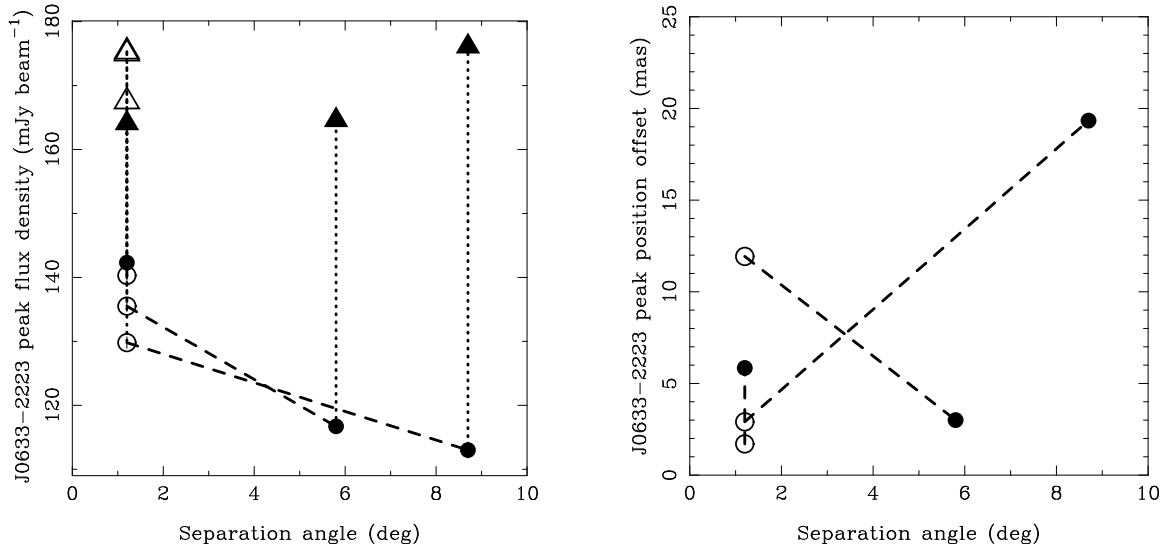


**Figure 11.** Compilation of the stage 3 Band 8–4 comparative study results as shown in Figure 10. Left: peak flux density of the J0633–2223 images. The horizontal axis is the separation angle to the phase calibrator. The filled and open circles represent the in-band and B2B phase referencing images, respectively. The triangles connected with the dotted lines represent their self-calibrated image. The **dashed** lines indicate the consecutive pairs of the B2B and in-band phase referencing observations. Right: peak position offset of the J0633–2223 images from the a priori phase tracking center.

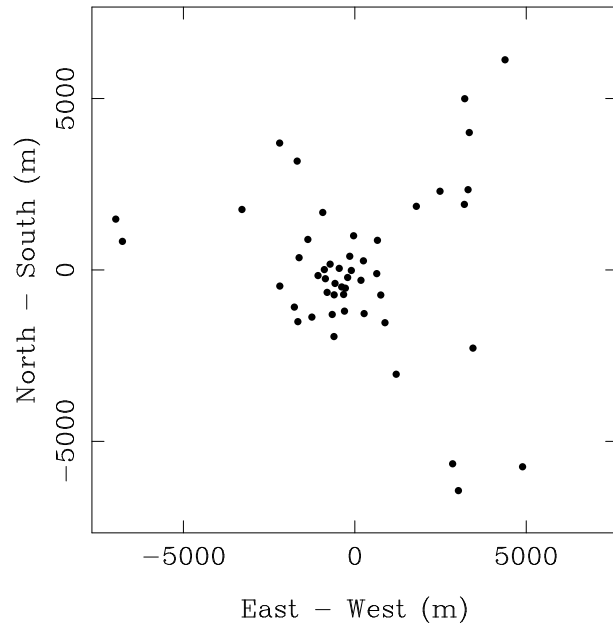


**Figure 12.** Array configuration on 2017 November 3 used for the stage 4 imaging test. The black circles represent the 12 m antenna position.

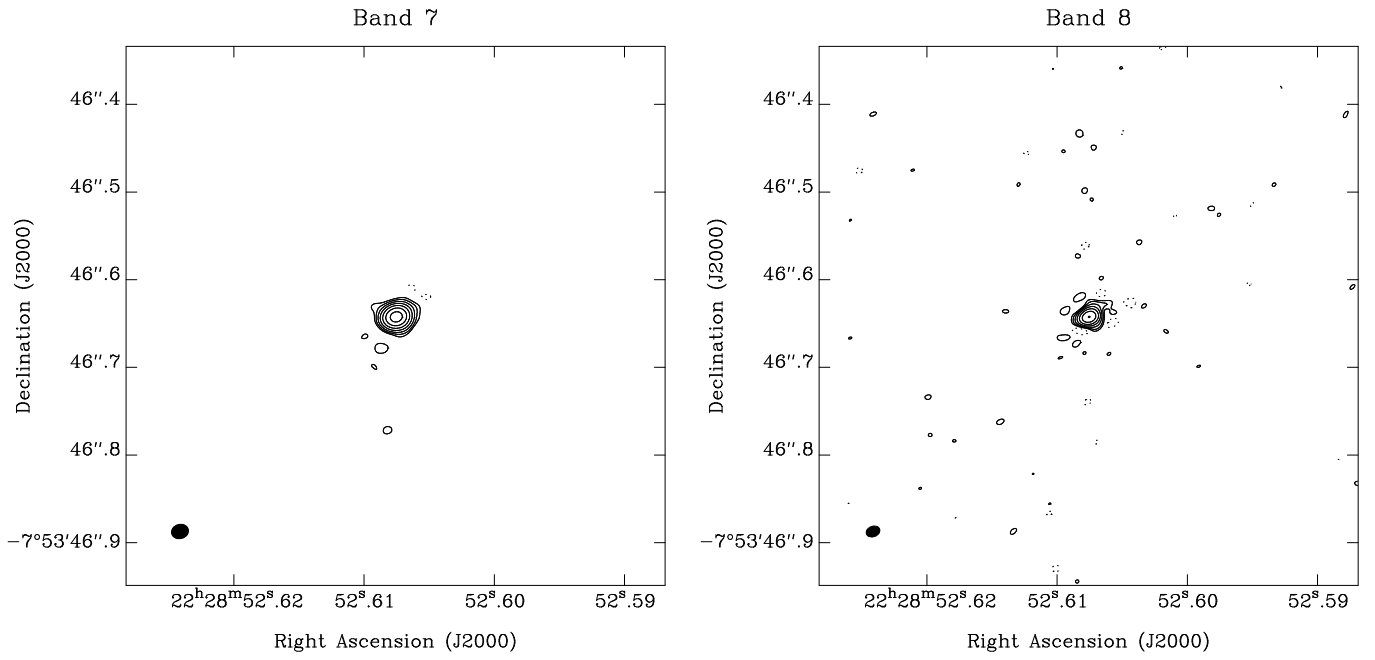


**Figure 13.** Continuum synthesis image of **QSO J2228–0753** calibrated with B2B phase referencing. The contours are drawn at  $-0.5, 0.5, 1.0, 2.0, 4.0, 8.0, 16.0,$  and  $32.0 \text{ mJy beam}^{-1}$  levels. The synthesized beam is shown in the bottom left corner of each panel. Left: Band 7 map using the Band 3 phase calibrator. The synthesized beam size with Briggs weighting ( $\text{robust}=0.5$ ) is  $19 \times 16 \text{ mas}$ . The peak flux density and image RMS noise are  $45.32$  and  $0.10 \text{ mJy beam}^{-1}$ , respectively. Right: Band 8 map using the Band 4 phase calibrator. The synthesized beam size is  $16 \times 12 \text{ mas}$ . The peak flux density and image RMS noise are  $32.35$  and  $0.16 \text{ mJy beam}^{-1}$ , respectively.

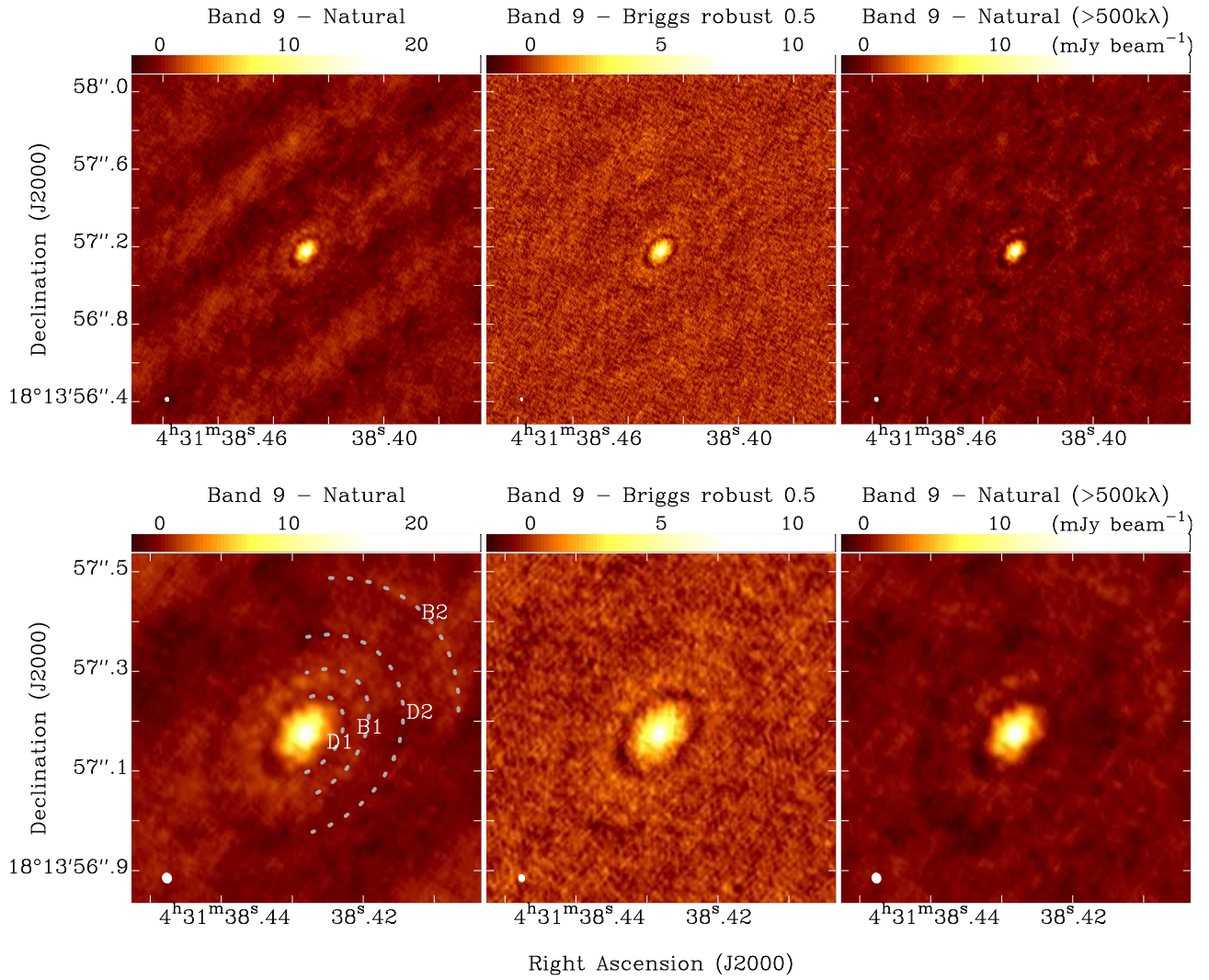


**Figure 14.** Top left: Band 9 continuum map of HL Tau calibrated with B2B phase referencing. The resulting beam is  $20 \times 18$  mas using a natural weighting. Top middle: same as left but where a Briggs robust image weighting of 0.5 is used so that the resolution is increased to  $14 \times 11$  mas. Top right: same as left but including baselines  $> 500$  k $\lambda$  only. The beams are shown in the bottom left corner. Bottom row: Enlarged area of the central  $700 \times 700$  mas of the top three images. The color gradation is modified from a linear scale to highlight the fainter emission.

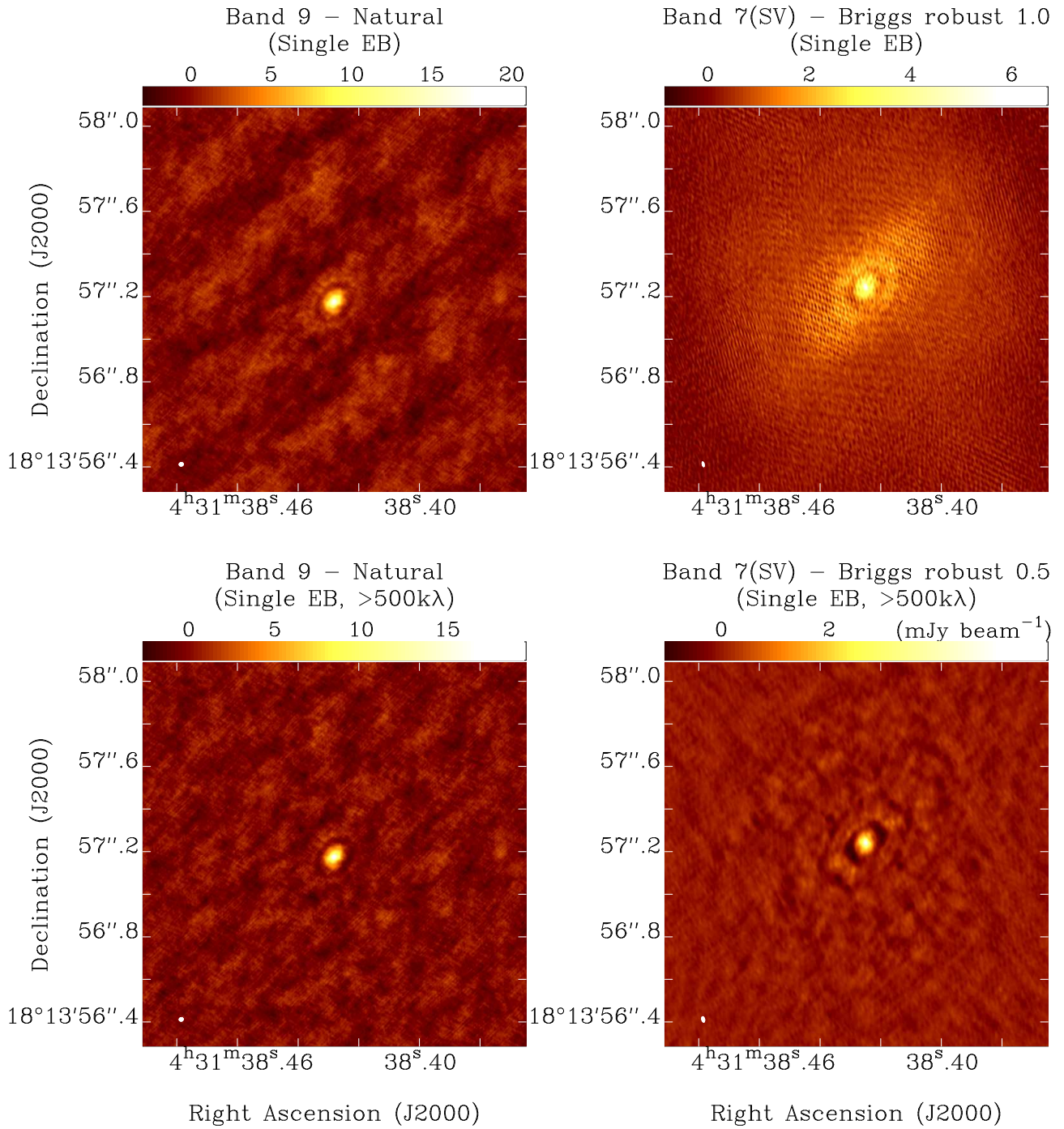


**Figure 15.** Top left: Band 9 continuum map of HL Tau from one EB only, calibrated with B2B phase referencing. Top right: Band 7 continuum map of HL Tau using only one EB from LBC-2014-SV. Bottom left: same as top left except imaged using only baselines  $>500\text{ k}\lambda$ . Bottom right: same as top right except imaged using robust 0.5 and only baselines  $>500\text{ k}\lambda$ . The beams are shown in the bottom left corner.



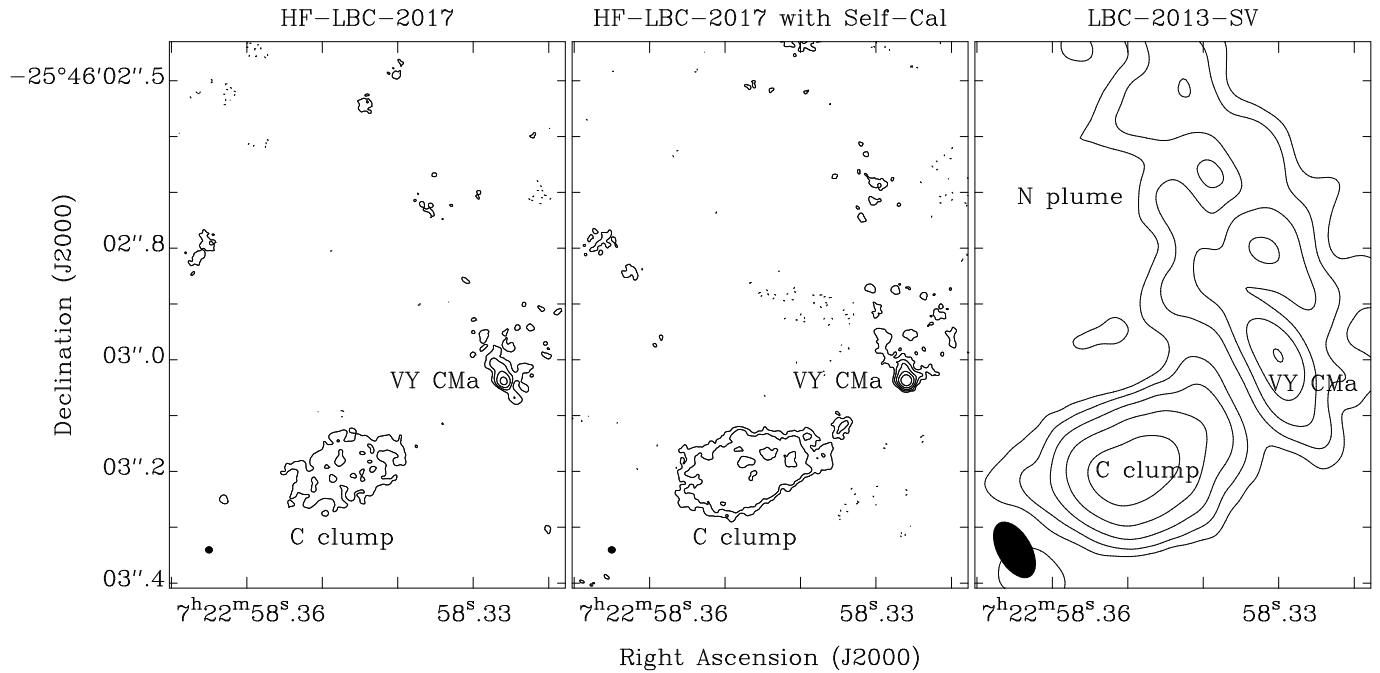


**Figure 16.** Band 9 continuum maps of VY CMa. The synthesized beam is shown in the bottom left corner of each panel. The contours are drawn at  $-3\sigma$ ,  $3\sigma$ ,  $6\sigma$ ,  $12\sigma$ ,  $24\sigma$ , and  $48\sigma$  levels. Left: HF-LBC-2017 image without self-calibration with a longest projected baseline length of 13.8 km. The synthesized beam size is  $12 \times 11$  mas with Briggs weighting (robust=2). The peak flux density and image RMS noise are  $41.5$  and  $1.4$   $\text{mJy beam}^{-1}$ , respectively. Middle: The same as the left panel but with self-calibration. The peak flux density and image RMS noise are  $135.5$  and  $1.5$   $\text{mJy beam}^{-1}$ , respectively. Right: ALMA SV data taken in 2013 with a  $B_{\text{max}}$  of 2.7 km. Note that the brightest peak is located not at VY CMa but in the C clump ( $316.0$   $\text{mJy beam}^{-1}$ ). The synthesized beam size is  $110 \times 59$  mas. The image RMS noise is  $4.1$   $\text{mJy beam}^{-1}$ .

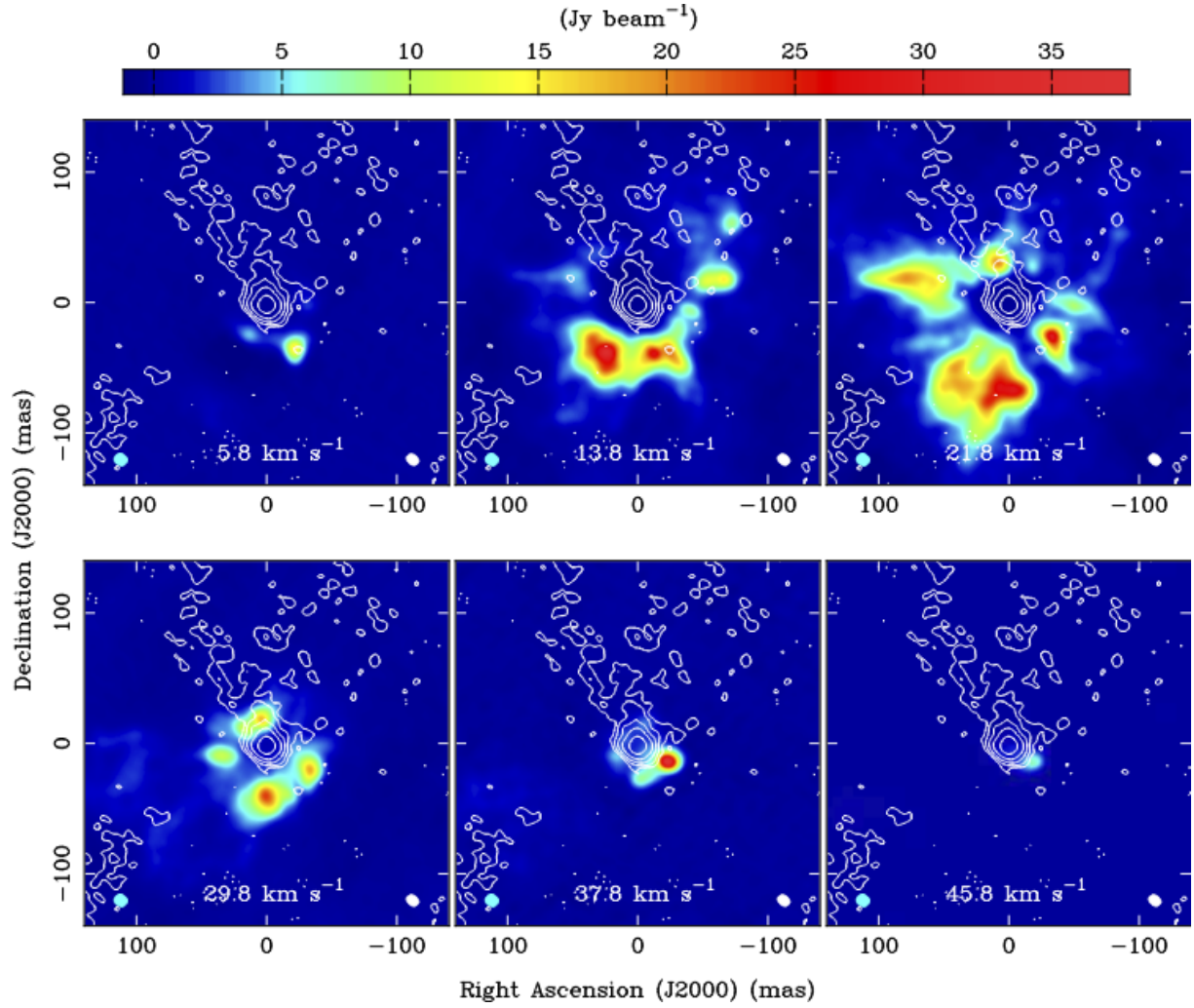


**Figure 17.** The 658 GHz H<sub>2</sub>O maser cube of VY CMA (color gradation) with Briggs weighting (robust=0.5) for a  $0.''28 \times 0.''28$  region. The synthesized beam size is  $10 \times 8$  mas, as displayed in the bottom left corner by a filled cyan ellipse. The map origin is centered on  $(\alpha, \delta) = (07^{\text{h}}22^{\text{m}}58^{\text{s}}.326, -25^{\circ}46'03''.038)$  in J2000. Each map was made by integrating the emission over a velocity width of  $8 \text{ km s}^{-1}$ . The radial velocity in LSRK is shown in the bottom in each map. The Band 9 continuum emission map with Briggs weighting (robust = 0) is also displayed with the white contours of  $2\sigma$ ,  $4\sigma$ ,  $8\sigma$ ,  $16\sigma$ ,  $32\sigma$ , and  $64\sigma$  ( $1\sigma = 1.8 \text{ mJy beam}^{-1}$ ), and the synthesized beam is displayed in the bottom right corner by a filled white ellipse.

**Table 1.** Possible Frequency Combination for the Harmonic Frequency Switching

HF Band	(LO1 Frequency Range)	LF Band	(LO1 Frequency Range)	LO1 Frequency Ratio
Band 7	(282.9 – 324.0 GHz)	Band 3	(94.3 – 108.0 GHz)	3
Band 8	(399.0 – 465.0 GHz)	Band 4	(133.0 – 155.0 GHz)	3
Band 8	(442.2 – 492.0 GHz)	Band 6	(221.1 – 246.0 GHz)	2
Band 9	(610.2 – 697.5 GHz)	Band 4	(135.6 – 155.0 GHz)	4.5
Band 9	(663.3 – 711.9 GHz)	Band 6	(221.1 – 237.3 GHz)	3
Band 10	(828.0 – 942.3 GHz)	Band 3	(92.0 – 104.7 GHz)	9
Band 10	(794.7 – 913.5 GHz)	Band 5	(176.6 – 203.0 GHz)	4.5
Band 10	(848.7 – 942.3 GHz)	Band 7	(282.9 – 314.1 GHz)	3

**Table 2.** Prohibited Frequency Range in the Harmonic Frequency Switching

HF Receiver	LO1 Frequency Range
Band 7	324 – 365 GHz
Band 8	393 – 399 GHz

**Table 3.** HF-LBC-2017 Stage 2 Experiments Reported in This Paper

Date	Baseline Range	Band <sup>1</sup>	DGC Source	EB (uid://A002/)
2017 Apr 11	15–396 m	7–3	J0006–0623, J2232+1143, 3C454.3, J0108+0135, J2348–1631	Xbeef47/X20e6
2017 Apr 23	15–460 m	9–6	J1924–2914, J1517–2422, J1604–4441 <sup>2</sup> , J1751+0939 <sup>2</sup> , J1337–1257 <sup>2</sup>	Xbf894a/X1aab, Xbf894a/X1c1e, Xbf894a/X1d58, Xbf894a/X1e87, Xbf894a/X1f9a
2017 May 4	17–1110 m	8–4	J0510+1800, J0522–3627, J0006–0623 <sup>3</sup> , J0450–8101 <sup>3</sup>	Xbff114/X2bc9

<sup>1</sup> HF Band for the target-LF Band for the phase calibrator.<sup>2</sup> The DGC solutions were not fully analyzed because of an antenna shadowing effect for low elevation angles.<sup>3</sup> The DGC solutions were not fully analyzed because the S/Ns were not high enough.

Table 4. HF-LBC-2017 Stage 3 Experiments Reported in This Paper

Date	Baseline Range	Band	Target	Phase Cal.	DGC Source	EB (nid://A002/Xc23361/)
2017 July 18	17–3697 m	8–4	J0633–2223	J0634–2335	J0522–3627	X4970, X4a9a, X4d1e, <sup>2</sup> X4e7c, <sup>2</sup> X5197, X52bb, X5550, X56b4
						X4865, X4b27, X4bd4, X4f11, X5053, X5355, X5402, X57c9
		8–8 <sup>1</sup>	J0633–2223	J0634–2335		X48f1, X49e9
				J0620–2515 <sup>2</sup> J0648–1744 J0609–1542		X4c81 <sup>2</sup> X4d1bb <sup>2</sup> X5105, X5213 X54a3, X55e9

<sup>1</sup> In-band phase referencing.<sup>2</sup> Executions failed because the target passed close to zenith.

**Table 5.** HF-LBC-2017 Stage 4 Experiments Reported in This Paper

Date	Baseline Range	Band	Target	Phase Cal.	DGC Source	EB (uid://A002/)
2017 Oct 9	41–14969 m	8–4				Xc5802b/X5bb.3
2017 Oct 10	233–16196 m	7–3		J2229–0832		Xc59134/Xd47
2017 Nov 2	222–13894 m	7–3	J2228–0753		J2253+1608	Xc65717/X56f
		8–4				Xc660ef/X8e0
2017 Nov 3	230–13894 m	9–4	HL Tau	J0431+1731		Xc660ef/X1b89, X660ef/X2046
			VY CMa	J0725–2640	J0522–3627	X660ef/X2d26

**Table 6.** Assumed Parameters for Phase Calibrator Scan

Scan duration	8 s
Antenna number	43
Required S/N (per scan)	$20 \times R$
Bandwidth (Bands 3–8)	7.5 GHz (1.875 GHz $\times$ 4 SPWs)
Bandwidth (Bands 9 and 10)	15 GHz (1.875 GHz $\times$ 8 SPWs)
SEFD (Band 3)	2167 Jy
SEFD (Band 4)	2709 Jy
SEFD (Band 5)	3221 Jy
SEFD (Band 6)	3221 Jy
SEFD (Band 7)	5662 Jy
SEFD (Band 8)	10,932 Jy
SEFD (Band 9)	36,171 Jy
SEFD (Band 10)	75,958 Jy



**Table 7.** Required Phase Calibrator Flux Density and Mean Separation Angle for B2B Phase Referencing

Target Band (LO1 (GHz))	Phase Cal. Band (LO1 (GHz))	Required Flux Density for Phase Cal. (Jy)	Mean Separation Angle (deg)
Band 7 (321)	Band 3 (107)	0.0957	3.1
Band 8 (405)	Band 4 (135)	0.120	3.5
Band 8 (470)	Band 6 (235)	0.0948	3.6
Band 9 (681)	Band 4 (151)	0.180	4.1
Band 9 (681)	Band 6 (227)	0.142	4.1
Band 10 (873)	Band 3 (97)	0.287	4.3
Band 10 (873)	Band 5 (194)	0.213	4.6
Band 10 (873)	Band 7 (291)	0.250	5.4

**Table 8.** Required Phase Calibrator Flux Density and Mean Separation Angle for In-band Phase Referencing

Target Band (LO1 (GHz))	Phase Cal Band. (LO1 (GHz))	Required Flux Density for Phase Cal. (Jy)	Mean Separation Angle (deg)
Band 7 (321)	Band 7 (321)	0.0834	3.7
Band 8 (470)	Band 8 (470)	0.161	5.0
Band 9 (681)	Band 9 (681)	0.376	7.8
Band 10 (873)	Band 10 (873)	0.792	12.6